

## Comparisons between Measurements in Regions of Laminar Shock Wave Boundary Layer Interaction in Hypersonic Flows with Navier-Stokes and DSMC Solutions

**Michael S. Holden, Timothy P. Wadhams**  
Aerothermal and Aero-Optics Evaluation Center  
Buffalo, New York 14225  
USA

**John K. Harvey**  
Department of Aeronautics  
Imperial College of Science, Technology and Medicine  
London 2BY 5LU  
UK

**Graham V. Candler**  
University of Minnesota  
Minneapolis, Minnesota 55455  
USA

### **ABSTRACT**

*Experimental studies were conducted in conjunction with computations in a code validation exercise to examine the ability of DSMC and Navier-Stokes techniques to predict the complex characteristics of regions of shock/shock and shock/ boundary layer interactions in hypervelocity flows. In the experimental program, detailed heat transfer and pressure measurements in laminar regions of shock wave/boundary layer interaction, and shock/shock interaction, over hollow cylinder/flare and double cone configurations in hypersonic flow. The experimental studies were conducted for a Mach number range from 10 to 12 with Reynolds numbers from  $1 \times 10^4$  to  $5 \times 10^5$  and stagnation temperatures from 2,000 °R to 5,000 °R. Miniature high-frequency thin-film and piezoelectric instrumentation were employed to obtain the high spatial resolution required to accurately define the distribution of heat transfer and pressure in the strong gradients which occur in regions of shear layer reattachment and shock/shock interaction. The program reported here was conducted in two phases. In the first phase of the code validation study, measurements and “blind” computations were made over complete hollow cylinder/flare and double cone configurations in high-temperature flows at Mach 10 and 12 for a range of freestream Reynolds numbers. In the second phase of the program, detailed heat transfer and pressure measurements were made over an extensive range of Reynolds number and total enthalpy conditions using only the hollow cylinder and the 25° conical segment of the models tested earlier in phase I. The selection of the freestream conditions employed in this second phase of the program was performed in conjunction with computations of the contoured nozzle flows and the flows over the two simple model configurations. Based on the results of the latter studies, we validated the computational schemes used to predict the properties of the freestream developed in the test section of the tunnel. Using these validated calculations, we have re-evaluated the comparisons made earlier between measurements on the double cone and hollow cylinder configurations and predictions made independently*

---

\* This work was supported by Internal Research and Development Funds by Calspan-UB Research Center (CUBRC) in conjunction with the Air Force Office of Scientific Research (AFOSR) programs in hypersonic research and code validation.

# Report Documentation Page

*Form Approved*  
*OMB No. 0704-0188*

Public reporting burden for the collection of information is estimated to average 1 hour per response, including the time for reviewing instructions, searching existing data sources, gathering and maintaining the data needed, and completing and reviewing the collection of information. Send comments regarding this burden estimate or any other aspect of this collection of information, including suggestions for reducing this burden, to Washington Headquarters Services, Directorate for Information Operations and Reports, 1215 Jefferson Davis Highway, Suite 1204, Arlington VA 22202-4302. Respondents should be aware that notwithstanding any other provision of law, no person shall be subject to a penalty for failing to comply with a collection of information if it does not display a currently valid OMB control number.

1. REPORT DATE <b>01 JAN 2006</b>	2. REPORT TYPE <b>N/A</b>	3. DATES COVERED <b>-</b>	
4. TITLE AND SUBTITLE <b>Comparisons between Measurements in Regions of Laminar Shock Wave Boundary Layer Interaction in Hypersonic Flows with Navier-Stokes and DSMC Solutions</b>		5a. CONTRACT NUMBER	
		5b. GRANT NUMBER	
		5c. PROGRAM ELEMENT NUMBER	
6. AUTHOR(S)		5d. PROJECT NUMBER	
		5e. TASK NUMBER	
		5f. WORK UNIT NUMBER	
7. PERFORMING ORGANIZATION NAME(S) AND ADDRESS(ES) <b>Aerothermal and Aero-Optics Evaluation Center Buffalo, New York 14225 USA</b>		8. PERFORMING ORGANIZATION REPORT NUMBER	
9. SPONSORING/MONITORING AGENCY NAME(S) AND ADDRESS(ES)		10. SPONSOR/MONITOR'S ACRONYM(S)	
		11. SPONSOR/MONITOR'S REPORT NUMBER(S)	
12. DISTRIBUTION/AVAILABILITY STATEMENT <b>Approved for public release, distribution unlimited</b>			
13. SUPPLEMENTARY NOTES <b>See also ADM001860, Technologies for Propelled Hypersonic Flight (Technologies des vols hypersoniques propulses). , The original document contains color images.</b>			
14. ABSTRACT			
15. SUBJECT TERMS			
16. SECURITY CLASSIFICATION OF:			17. LIMITATION OF ABSTRACT <b>UU</b>
a. REPORT <b>unclassified</b>	b. ABSTRACT <b>unclassified</b>	c. THIS PAGE <b>unclassified</b>	
			18. NUMBER OF PAGES <b>56</b>
			19a. NAME OF RESPONSIBLE PERSON

*with Navier-Stokes and DSMC predictive schemes. These studies demonstrate that correctly calculating the effects of vibrational nonequilibrium in the freestream properties improve the already excellent agreement between the prediction techniques and experimental data.*

## 1 INTRODUCTION

The increased stability of a laminar boundary layer under hypersonic flow conditions results in a situation where extensive regions of laminar flows will occur over hypersonic re-entry and air-breathing vehicles. Therefore, it is possible to obtain accurate predictions of the laminar aerothermal loads with Navier-Stokes and DSMC calculations. However, these methods must be employed carefully in describing regions of separated flows induced by shock/boundary layer interaction and in the strong gradients generated in regions of shock/shock interaction. Here the accuracy of the predictions can be strongly influenced by the differencing schemes and gridding techniques employed in the computation of regions of strong pressure gradients and recirculating flows. However, to describe such regions in hypervelocity flows, it is necessary to introduce models of the flowfield internal energy exchange and chemistry and the flow surface interaction in regions close to the leading edge. This is true even for nitrogen hypervelocity flows where vibrational nonequilibrium can influence both the properties of the freestream and over the model.

During the past decade, there have been significant efforts in Europe and America to validate the prediction techniques employed in the new classes of re-entry and air-breathing vehicles. Extensive code validation activities were conducted in conjunction with European space activities in the 1990s, and similar activities were conducted in the United States, in support of space vehicle design including those developed in the NASP program. A combined American/European code validation exercise was promoted by the NATO Research Technology Organization (RTO) under Working Group 10. Also working with the support of the Air Force Office of Scientific Research (AFOSR), a number of experimental and numerical studies were conducted to examine complex viscous/inviscid interaction regions developed over simple model configurations in laminar hypersonic flows. During these studies, two model configurations – a hollow cylinder flare and a double cone configuration – emerged as simple configurations over which complex interacting flows are developed which can provide a stringent test to the numerical schemes that are employed in the Navier-Stokes and DSMC computations. Early experimental studies using a hollow cylinder/flare configuration were conducted in France by Chanetz et al (Ref. 1), and were compared with extensive series of computations employing Navier-Stokes and DSMC methods. These studies revealed that the extent of the separated region was highly sensitive to grid selection, and discrepancies were also found between the measured and predicted pressure in the interaction regions. Similar comparisons between the computations of Olejniczak and Candler (Ref. 2) and Gnoffo (Ref. 3) with measurements over a double cone configuration (Holden, Ref. 4) also revealed significant numerical problems can be encountered when predicting the strong gradients generated in regions of shock/shock interaction and boundary layer separations where the differencing schemes can be prone to oscillation and the mesh generation and refinement schemes must be handled with care.

To investigate such problems further, a new set of experimental studies was initiated employing models similar to those used in the hollow cylinder/flare and the double cone experimental studies. The hypersonic low-density conditions were selected to avoid problems associated with boundary layer transition and provide an opportunity for both DSMC and Navier-Stokes techniques to be employed in predicting these flows. While the model configuration of the basic hollow cylinder cone geometry was preserved, experiments were conducted with an extended flare configuration to provide well-defined downstream boundary layer conditions for comparison with prediction schemes. For the double cone experiments, a  $25^\circ/55^\circ$  configuration was selected to avoid the potential of flow unsteadiness over the model; and again these studies were conducted at

Reynolds numbers low enough to ensure that the flow was laminar downstream of the interaction over the second cone.

The results of these experimental studies were presented at the 2001 AIAA Reno meeting in a session dedicated to Code Validation. In this session, the predictors were given only information on the freestream conditions and the model geometry to determine the aerothermal properties over the models tested. In this “blind” code validation study, the predictors first presented their data, with the comparisons between theory and experiment presented independently at the conclusion of the session (see Refs. 5 and 6). In general, the comparisons between theory and experiment were excellent. For example, the comparisons shown in Figure 1 demonstrate that the size of the separated region and the magnitude of the heat transfer and pressure distributions through the separated and reattachment region were in excellent agreement with the experimental measurements. Likewise, comparisons between the density contours obtained from the Schlieren photographs over the double cone configuration compared in Figure 2 with Candler’s predictions demonstrate almost perfect agreement. With the exception of the forebody flows the DSMC methods have not yielded as good an agreement as the Navier-Stokes method, which in part may be attributed to the high density of the flowfield in the reattachment region. Also, for complex dense flows, there are questions on the level of convergence of the solutions. The Navier-Stokes methods consistently overpredicted the heating rates over the forebody ahead of separation, potentially as a result of vibrational nonequilibrium and slip effects. Similar conclusions can be made for the comparisons between prediction and experiment over the hollow cylinder flare model. There again, questions arose concerning the modeling of the vibrational nonequilibrium in the freestream and slip effects near the leading edge of the models, which resulted in a second experimental measurement and numerical program to select the most effective techniques and analyses to determine the properties of the freestream in the presence of vibrational nonequilibrium.

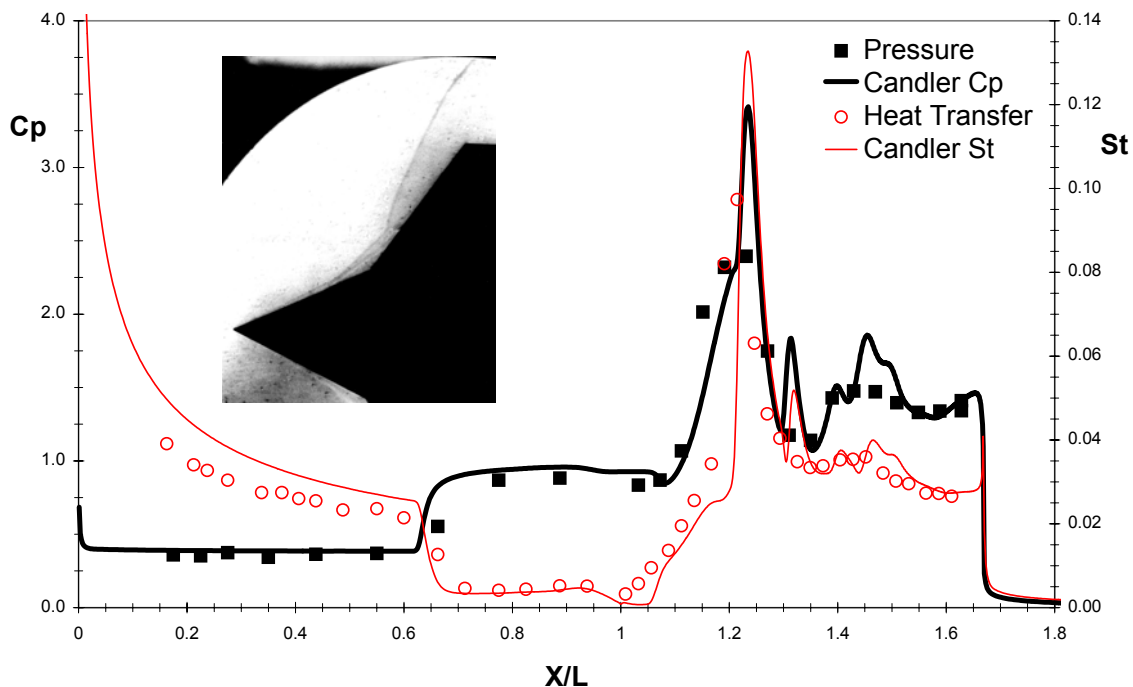


**Figure 1: Comparison between Heat Transfer and Pressure Measurement on  
Double Cone Model and Navier-Stokes predictions by Candler (Ref. 7).**

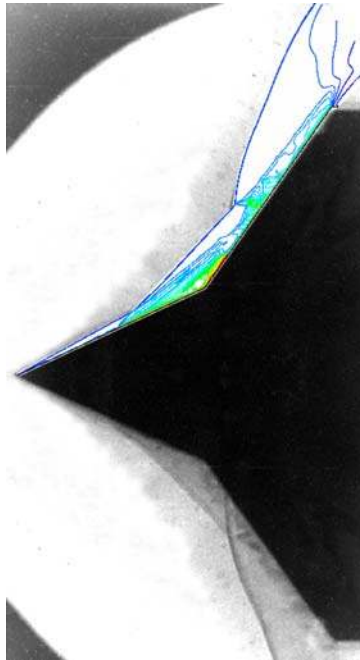


**Figure 2: Composite Picture Showing Density Contours from Candler's Solution for the Biconic Model Superimposed on a Schlieren image. (Run 24)**

In this paper we first discuss an additional set of experimental studies, conducted in conjunction with computations made by Candler (Ref. 7), to evaluate the effects of vibrational nonequilibrium of nitrogen in the freestream, thereby providing a more accurate definition of the freestream properties employed in the validation experiment. To validate the accuracy of the freestream properties deduced from the computational techniques employed at the Aerothermal and Aero-optic Evaluation Center (AAEC), and by Candler, measurements were made over the hollow cylinder detached from the flare and the 25° cone detached from the 55° conical second section of the model. Measurements were made over a large range of stagnation temperature and Reynolds numbers conditions to obtain conditions that varied from rarefied to continuum in the region of the leading edges, and where vibrational nonequilibrium was excited ( $T_0 = 5,000^\circ\text{R}$ ) as in the earlier experiments and unexcited ( $T_0 = 2,000^\circ\text{R}$ ) in colder flows in the freestream. The heat transfer and pressure measurements made in these studies were compared with detailed Navier-Stokes calculations and correlated in terms of the parameters used in simple predictive techniques. Also in these studies we examine the effect of levels of water vapor in the freestream on the calculations and on the experimental measurements. From this study, we validated the detailed and simple techniques, which are employed to describe the freestream conditions around the model in the presence of vibrational nonequilibrium of the test gas. Armed with these improved freestream conditions, we re-evaluated the comparisons between theory and experiment which were presented in Reno in 2001 (Refs. 5 and 6).

## **2 MEASUREMENTS MADE IN THE EXPERIMENTAL PROGRAM**

### **2.1 Design of the Experimental Program**

This experimental program was designed to obtain sets of surface heat transfer and pressure measurements and Schlieren photographs of the flowfield in complex shock/boundary layer and shock/shock interaction

regions over simple model configurations. From these, an experimental database is derived at low enough densities to evaluate the performance of Navier-Stokes and DSMC methods in predicting these stressing flows. Two model configurations, a hollow cylinder/flare and a double cone model, were selected for these studies based on the experience obtained in earlier experimental studies and code validation exercises. The interest in the flow over the hollow cylinder/flare configuration stems from earlier computational difficulties, which arose from rarefaction and shock interaction effects near the leading edge, and the complexity of the flow in the recirculation region. The short flare length selected for these earlier studies (see Ref. 1) did not allow a well-defined attached boundary layer to be developed downstream of the attachment and there is a possibility of forward propagation of disturbances from the base region. The configuration thus does not provide an optimal set of boundary conditions, and the flow is not ideal for comparison with computation. In the current studies we chose to move the end of the flare well downstream of the reattachment, thereby providing a well-defined boundary condition, which would anchor both experimental and theoretical measurements.

Earlier studies with double cone configurations, which were conducted principally to assess the accuracy of the models of flowfield chemistry, employed cone angles, which could potentially lead to oscillations in the flow over the model. Such instabilities were observed in numerical computations and their sources were not fully understood. To avoid these instabilities in the current studies, we lowered the second cone angle to  $55^\circ$ , and the selection of this configuration was validated with computations by Gnoffo (Ref. 8). Again, the length of the second cone was selected to ensure that a region of near constant pressure existed downstream of the interaction region at the junction between the cones and the shear layer impingement resulting from shock/shock interaction. Measurements were made for both sharp and blunted configurations, which would introduce significant flowfield chemistry effects if testing were to be conducted in air. For all the studies reported, we used nitrogen to avoid significant dissociation effects, however, at the highest enthalpies, vibrational nonequilibrium can influence the heating rate to the surface of the model. Measurements over the cylinder flare and double cone configurations were made over a range of Mach and Reynolds numbers to obtain well-defined attached flows upstream and downstream of the corner interaction regions and to examine the flow for any evidence of boundary layer transition at the back of the flare of the second cone.

In the second set of experimental studies, we examine vibrational nonequilibrium effects that were performed over 40 runs with just the hollow cylinder and the  $25^\circ$  section of the double cone model. These studies were conducted over a much larger range of Reynolds numbers (because we were no longer concerned with boundary layer transition) and total temperatures lower than the earlier studies with the complete configurations so we could vary independently the levels of vibrational nonequilibrium in the freestream and the leading edge interaction effects.

## 2.2 Models and Instrumentation

### 2.2.1 The Hollow Cylinder/Flare Configurations

A photograph of the hollow cylinder flare model employed in our studies is shown in Figure 3. As illustrated in Figure 4, a section of the flare is removable to turn this model into a configuration of the exact geometry of the model originally tested by Chanetz et al (Ref. 1). The length of the “extended flare” was selected based on calculations by Gnoffo to ensure that a well-defined length of constant pressure was obtained downstream of the interaction for the conditions at which we proposed to perform our experimental studies. The dimensions of the two models employed in our two studies are shown in Figure 4. Both models were highly instrumented with pressure and thin film heat transfer gages and positioned as illustrated in Figure 5. Instrumentation was also placed around the circumference of the flare to check for model alignment and any flow asymmetries.



The test conditions were selected to ensure that flow over the entire extended flare configuration remained fully laminar with sufficient measurements upstream and downstream of the interaction to define the boundary conditions.



Figure 3: Photograph of the Cylinder/Extended Flare Model.

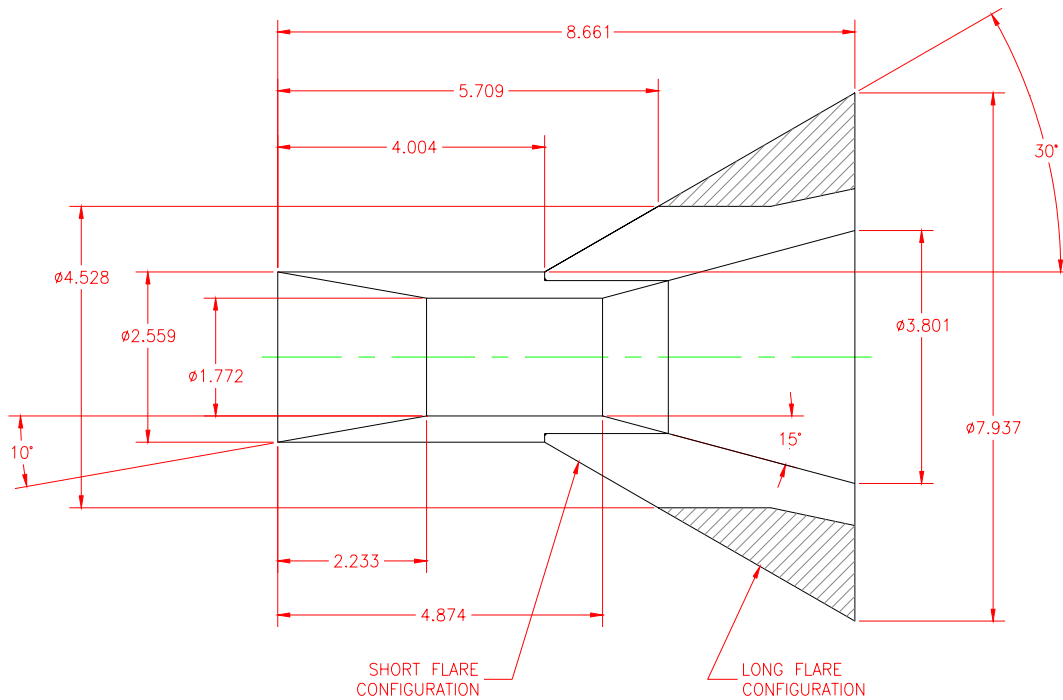
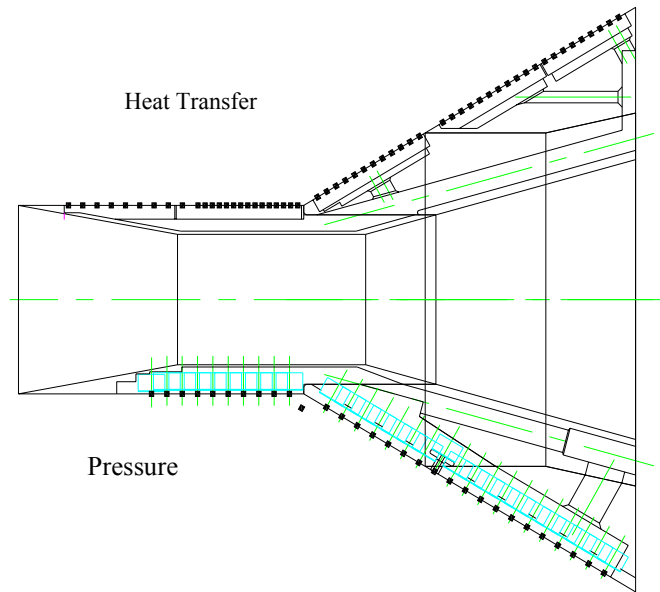
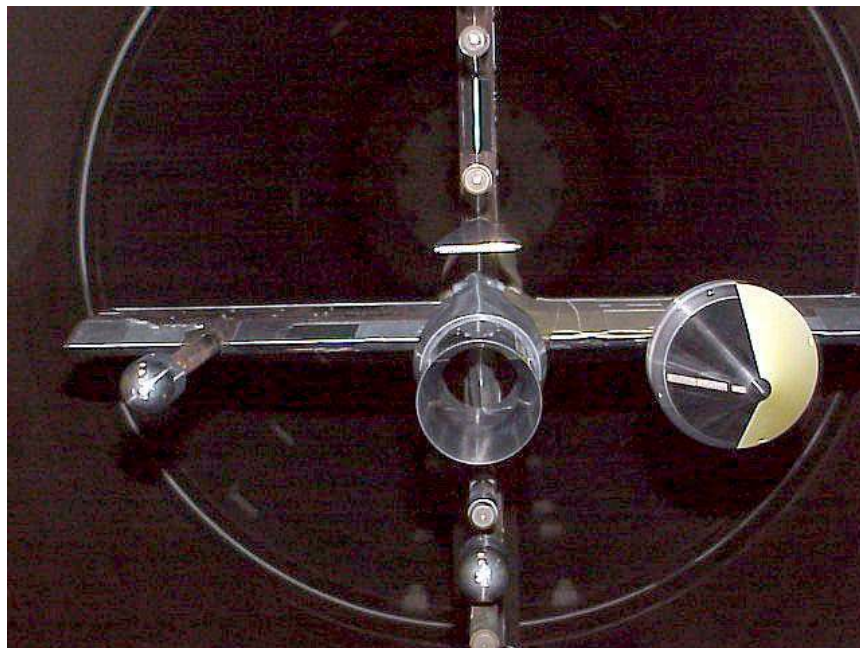


Figure 4: Dimensions for Two Cylinder Flare Configurations Employed in the Experimental Studies.



**Figure 5: Instrumentation Layout on Cylinder/Flare Models.**

In the studies to examine vibrational nonequilibrium effects, we replaced the flare section of the model with a cylindrical extension incorporating the model support system. The cylindrical section of the model was equipped with similar instrumentation employed with the cone/flare model. This model is shown installed in the calibration rake alongside the forebody of the double cone model in Figure 6.



**Figure 6: Hollow Cylinder Model Supported in Flowfield Rake Assembly.**



### 2.2.2 Sharp and Blunt Cone and Double Cone Configuration

The sharp  $25^\circ/55^\circ$  double cone model shown in Figure 7 was selected as the principal configuration to be employed in our studies based on evidence from our earlier experimental studies and numerical computations performed by Gnoffo, which indicated that the flow would be fully stable for all the freestream conditions at which the model was tested. A series of blunt nosetips were fabricated for the  $25^\circ$  cone to investigate the effects of bluntness on the size and character of the interaction region. Diagrams showing the dimensions of the four configurations tested are shown in Figure 8. Limited studies were performed with the  $25^\circ/60^\circ$  double cone configurations principally as a link to our earlier studies. Measurements were made with configurations shown in Figure 9, and again these flows were stable; however, only for the sharp configuration tested at our largest Mach number and lowest Reynolds number conditions did we obtain sufficient lengths of attached flow to meet our selection criteria.

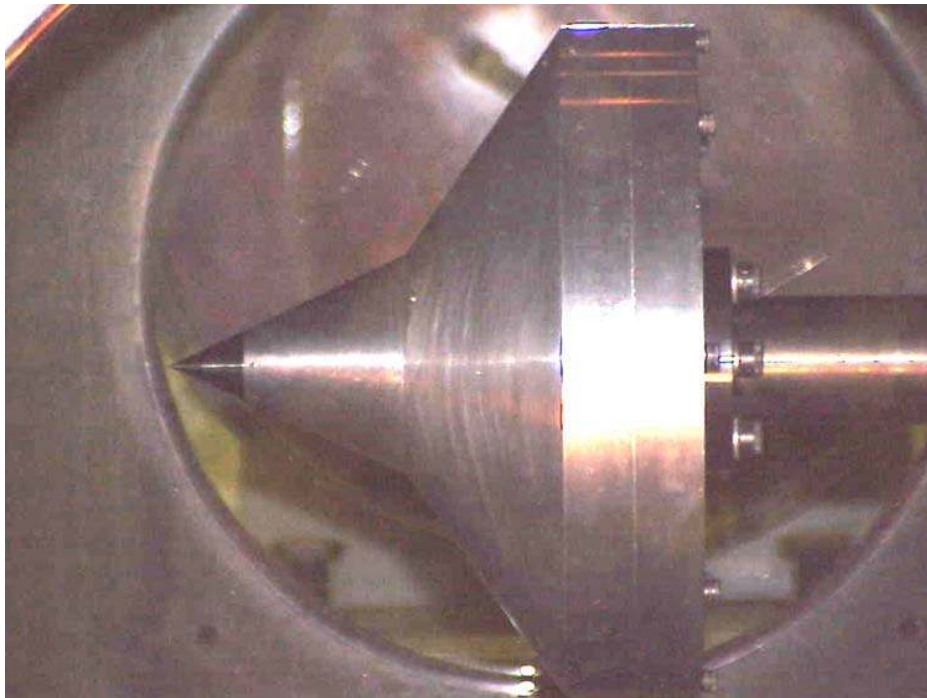


Figure 7: Photograph of Double Cone Model in LENS I Tunnel.

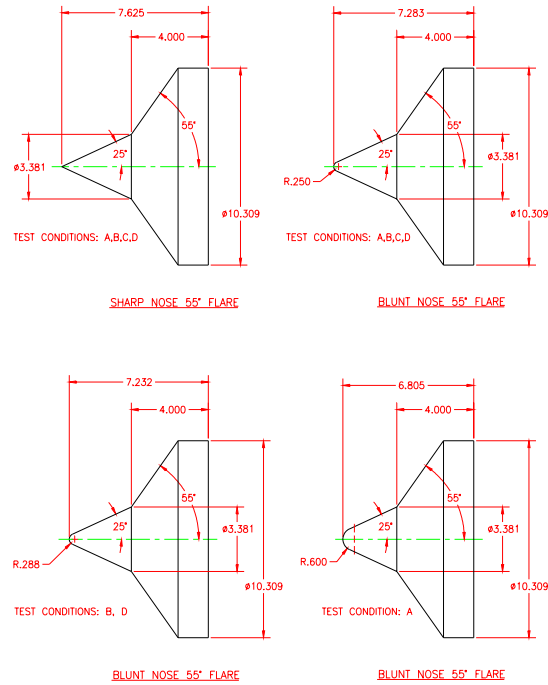


Figure 8: Sharp and Blunt 25°/55° Double Cone Configurations.

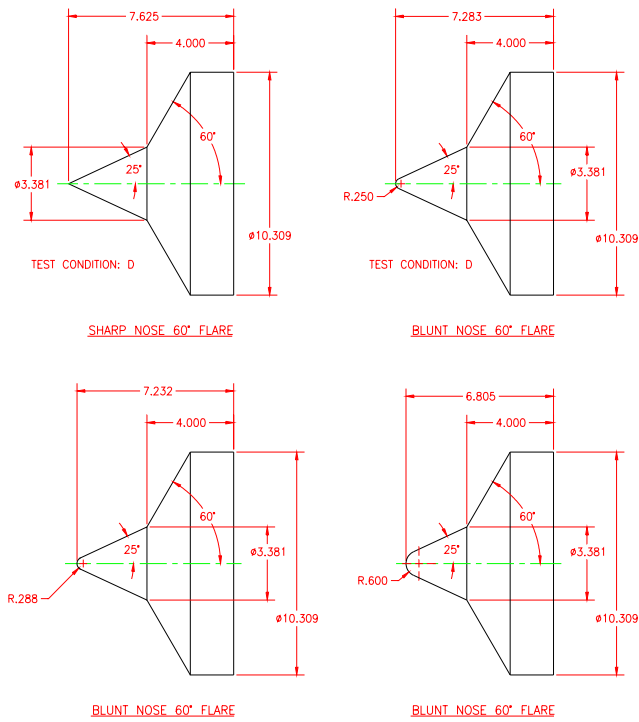


Figure 9: Sharp and Blunt 25°/60° Double Cone Configurations.

The double cone model was highly instrumented with heat transfer and pressure instrumentation as shown in Figure 10. The additional heat transfer instrumentation was placed in the 25° cone for the studies that we conducted with only this section of the model. A second cone was fabricated and also instrumented with heat transfer gages. The two cones were tested together and in some cases, a blunt nose was placed on one of these cones. A photograph of the two cones mounted on the calibration rake for the “vibrational nonequilibrium studies” is shown in Figure 11.

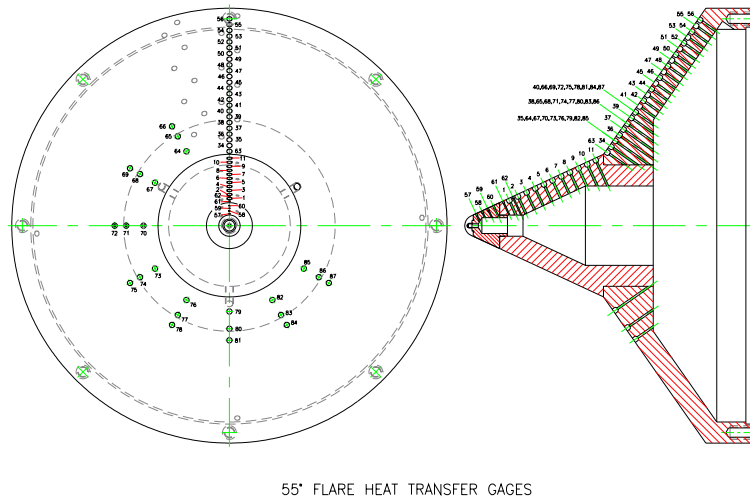


Figure 10: Distribution of Heat Transfer Gages on Double Cone Model.



Figure 11: Two 25° Cone Models in Survey Rake for “Vibrational Nonequilibrium” Studies.

### 2.2.3 Instrumentation Used in Survey Rakes

A photograph of a survey rake containing pitot-, static-, and cone-pressure probes, together with thin-film and Medtherm instrumented heat transfer probes, are shown in Figure 12. We employed Cornell Aeronautical Laboratory (CAL)-designed piezoelectric pressure transducers, and Endevco and Kulite strain gage transducers, in our pitot pressure static pressure, and cone pressure probes. Under high enthalpy conditions, we used specially developed heat shields ahead of the piezoelectric transducers used in the pitot pressure rake. Miniature Endevco and Kulite pressure gages are mounted close to the surface in our static pressure probes. The low-pressure piezoelectric instrumentation is capable of measuring pressures down to  $10^{-4}$  psia with accuracy of  $\pm 10\%$ , and we have obtained similar accuracy with the low-pressure Kulite and Endevco transducers. Stagnation point heat transfer measurements are made with both platinum thin-film and thermocouple coaxial heat transfer gages. We also make measurements around the hemispherical stagnation point heating probes. In these studies, we also added a small cylindrical stagnation point heat transfer gage depicted in Figure 12. In our studies radiation measurements were employed to determine the level of water vapor in the airflow. A photograph of the measurement head of one of these instruments is shown in Figure 13.



Figure 12: Survey Rake containing Pressure, Heat Transfer and Radiation Instrumentation.



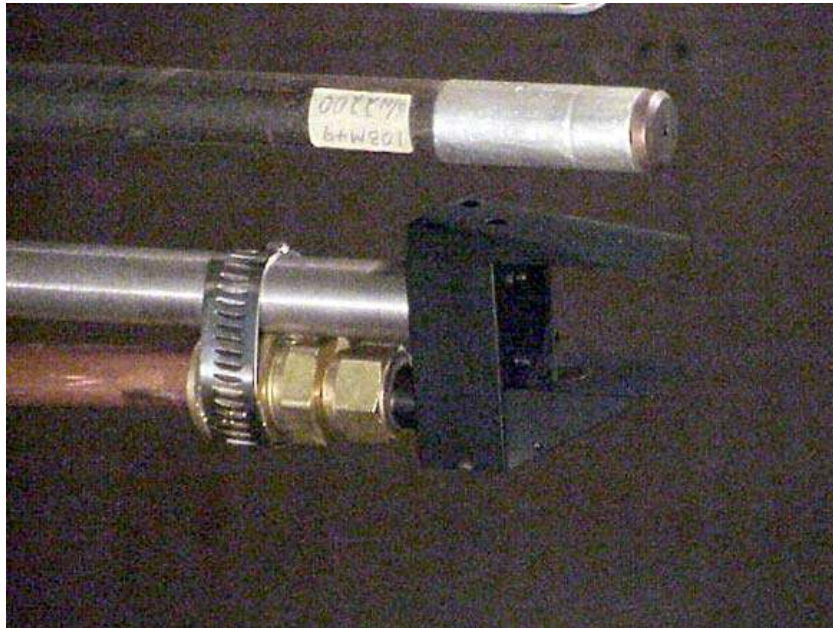


Figure 13: Water Vapor Measurement Sensor.

#### 2.2.4 High-Speed Schlieren Imagery with High Speed Video System

The low densities of the flowfields generated in these studies mandated that a double pass Schlieren system be employed. Schlieren images were obtained through the use of a pulsed copper vapor laser as the light source, and a high-speed video camera as the recording instrument. Since laser coherence effects are not desired in this application, the Oxford Lasers LS-20 copper vapor laser was operated without mirrors. Its light output was then delivered through 10 meters of fiber optic cable to further minimize coherence. The high-speed Kodak *Ektapro* camera was operated at the laser pulse frequency of 4,500 pulses per second. Thus, images were obtained throughout the complete run sequence, detailing flow start up, stable operation, and flow breakdown. Another distinct advantage for low-density measurements was the high intensity available from the laser source. The laser intensity was controlled through a variable neutral density filter. To achieve high Schlieren sensitivity, the knife-edge cut-off could be increased without fear of losing image illumination. In this way, the recorded contrast could be optimized for these flow density flow disturbances. Finally, because of the digital nature of the recorded images, simple software enhancement of the image contrast was utilized to produce the final images.

### 2.3 Test Facilities and Determination of Freestream Conditions

#### 2.3.1 Introduction

The capability to obtain accurate measurements in fully laminar regions of shock/shock and shock/ boundary layer interaction in hypervelocity flows requires the use of wind tunnel facilities capable of generating high-quality, high-temperature, low Reynolds number flows. Over the past 40 years, since the development of the shock tunnel at CAL, a concerted effort has been made in our laboratory to develop and use these facilities and the associated tunnel and model instrumentation in fundamental studies in low Reynolds number shock/boundary layer interacting flows, with and in the absence of flowfield chemistry for the purpose of

developing and validating the prediction techniques. The 48-inch tunnel developed at CAL has been proven over its 40-year history to generate high-quality low Reynolds number flows, and the measurements made in the facility have been validated by flight tests from the Gemini to the space shuttle as well as in comparisons with well-established prediction techniques. The design of the LENS I facility incorporates many of the key features learned from our earlier facility development, as well as improvements in the tunnel components and a significant increase in the high-pressure, high-enthalpy (2,000 atm/12 MJ/kg) and test time performance of the tunnels. These tunnels are being employed in our Verification, Validation and Analysis (VV&A) programs for both facility and code validation, with the effort centered initially on comparing measurements in complex regions of shock wave/laminar boundary layer interaction and separated flows developed on models tested in these facilities with the most current sophisticated prediction techniques.

### 2.3.2 Experimental Facilities

#### *48-inch Shock Tunnel*

We employed the 48-inch shock tunnel first in the studies with the double cone model configurations and subsequently in the studies with the hollow cylinder and 25° cone model. A photograph of the double cone model mounted in the test section of the 48-inch tunnel is shown in Figure 14. Shown in Figure 6 is a photograph of the hollow cylinder/flare and 25° cone model supported in the survey rake for the vibrational nonequilibrium studies. A schematic diagram of the operation is shown in Figure 15. The 48-inch shock tunnel (and the LENS facility discussed below) is basically a “blow-down tunnel” with a shock-compression heater. The flow through the tunnel is initiated by rupturing a double diaphragm, permitting high-pressure gas in the driver section to expand rapidly into the driven section. This generates a normal shock, which propagates through the gas in the driven tube, where it is heated and compressed. A region of high-temperature, high-pressure air is produced between this normal-shock front and the gas interface (often referred to as the contact surface). When the incident shock strikes the end of the driven section, it is reflected, leaving a region of almost stationary, high-pressure, heated air. This reservoir gas is then expanded through a nozzle to the desired freestream conditions in the test section. The duration of the flow in the test section is controlled by the interactions between the reflected shock, the driver/driven-gas interface, and the leading expansion wave generated by the non-stationary expansion process occurring in the driver section. We control the initial conditions of the gases in the driver and driven sections so that the gas interface becomes transparent to the reflected shock, which is referred to as operating under “tailored-interface” conditions. In preparation for the double cone studies flowfield calibrations were performed for the specific test points at which the experimental studies were conducted. A typical distribution of Mach number across the exit plane of the 48-inch “D” Nozzle obtained in the earlier calibration run is shown in Figure 16, which demonstrates excellent flow uniformity across the model width.



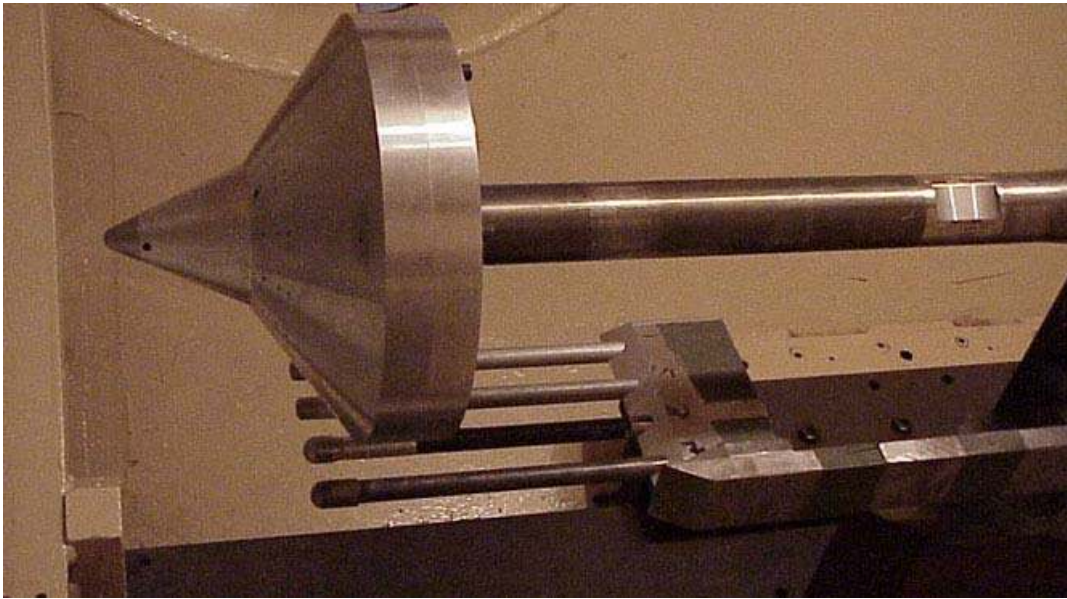


Figure 14: Photograph of Double Cone Model and Test Condition Rake Installed in 48” Tunnel.

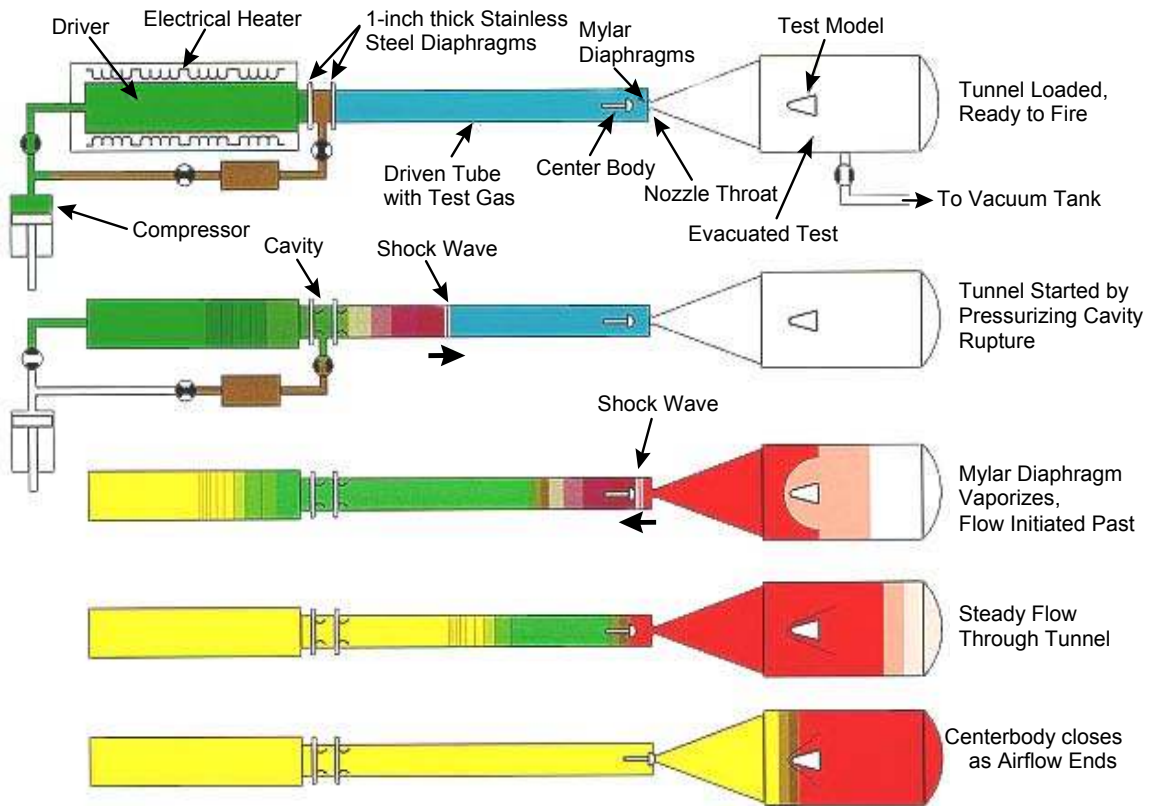
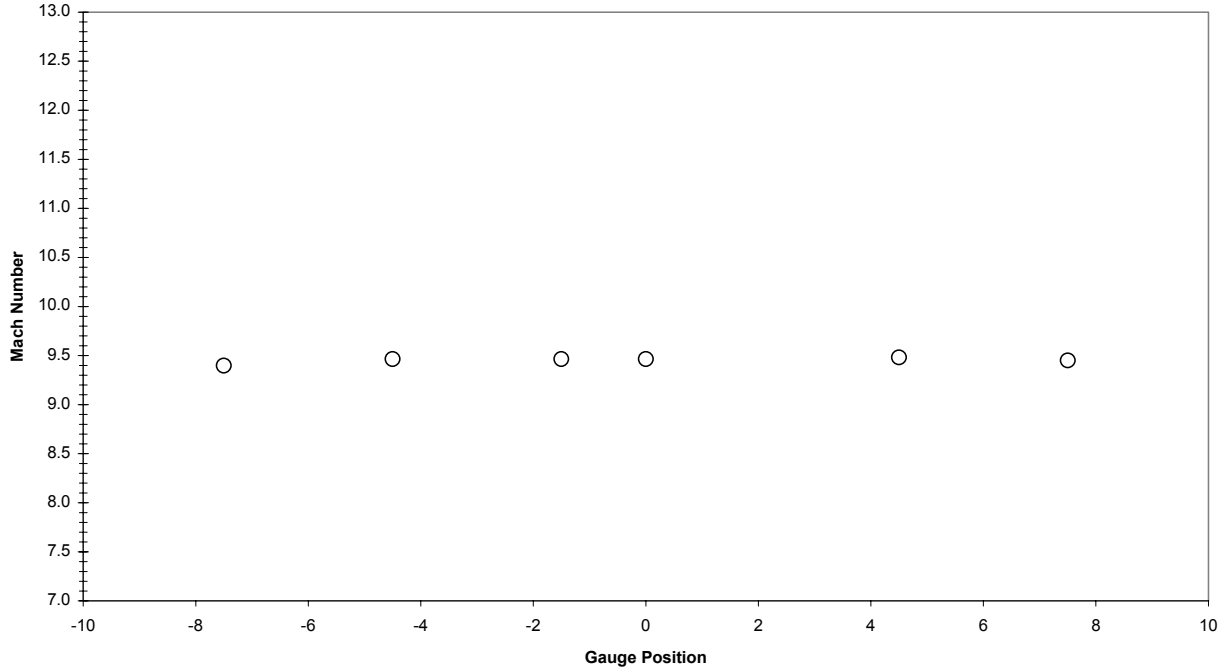


Figure 15: Schematic Diagram Illustrating the Operation of the 48” and LENS Shock Tunnels.



**Figure 16: Mach Number Distribution Across Exit Plane of "D" Nozzle from Survey Rake Measurements.**

### *LENS I Shock Tunnel*

We employed the LENS I facility in the studies of both the double cone and hollow cylinder/flare programs. We began our studies in the LENS I tunnel by repeating several sets of measurements made earlier in the 48-inch tunnel with the 25°/55° double cone configuration, as part of our facility-to-facility validation program. A photograph of the test section, nozzle and driven sections of the LENS I and II shock tunnels are shown in Figure 17. We then used a model with temperature-sensitive paint to obtain measurements to evaluate the symmetry of the flow in the separated region. All the hollow cylinder/ flare studies were conducted in the LENS I facility. A photograph of the hollow cylinder/flare model with the total pressure and heat transfer rakes supported below it are shown in Figure 18. The layout of facilities supporting Legs I and II of the LENS facility are shown schematically in Figure 19. Nitrogen, helium and hydrogen can be employed as driver gases allowing tailored interface operations up to a velocity of 14,000 ft/sec. The LENS I facility has two contoured nozzles allowing it be operated over a range from Mach 7 to 18 (see Figure 20). Test times of up to 24 milliseconds can be obtained at velocities from 3,000 to 15,000 ft/sec. in this tunnel. Both LENS Leg I and Leg II are operated under tailored interface conditions by carefully controlling the operating parameters and the gases employed in the driver and driven tubes. The Mach 8 and 14 nozzles for LENS Leg I have exit plane diameters of 44 and 48 inches, respectively, which allow the installation of models of up to 24 inches in diameter and 12 feet long.

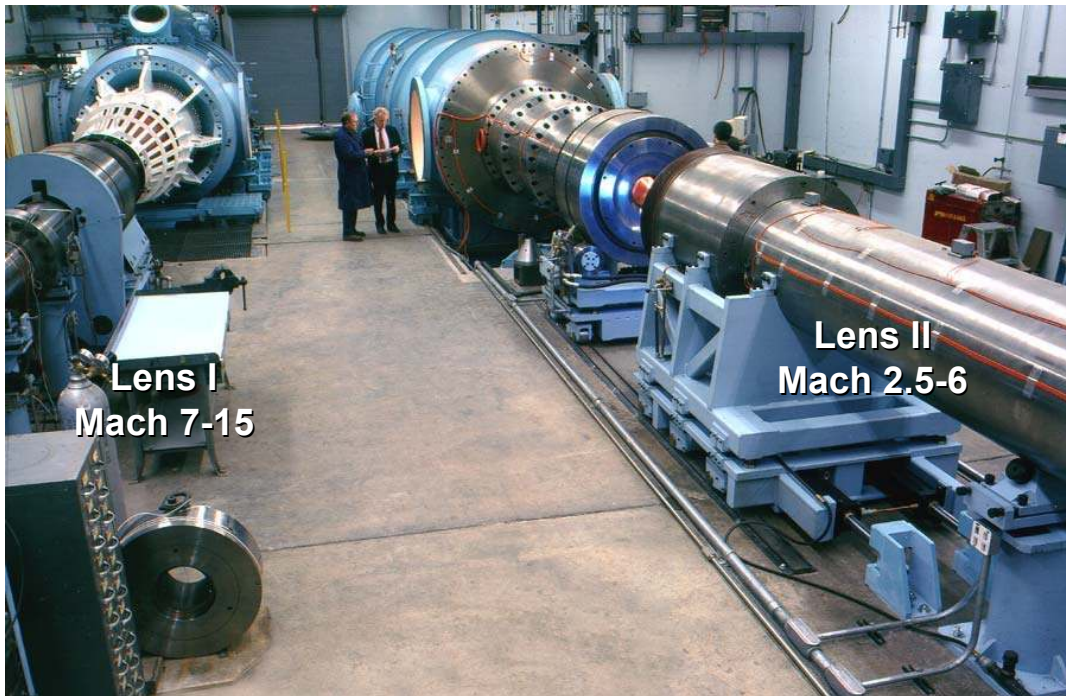


Figure 17: Photograph of LENS I and II Test Facilities.

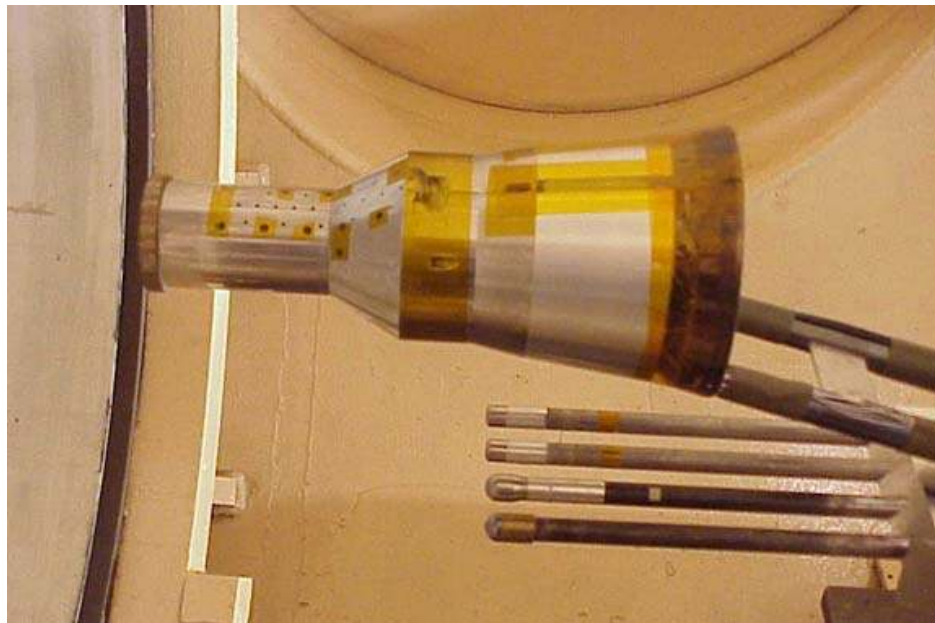


Figure 18: Hollow Cylinder Flare and Test Condition Rake Installed in LENS Shock Tunnel.



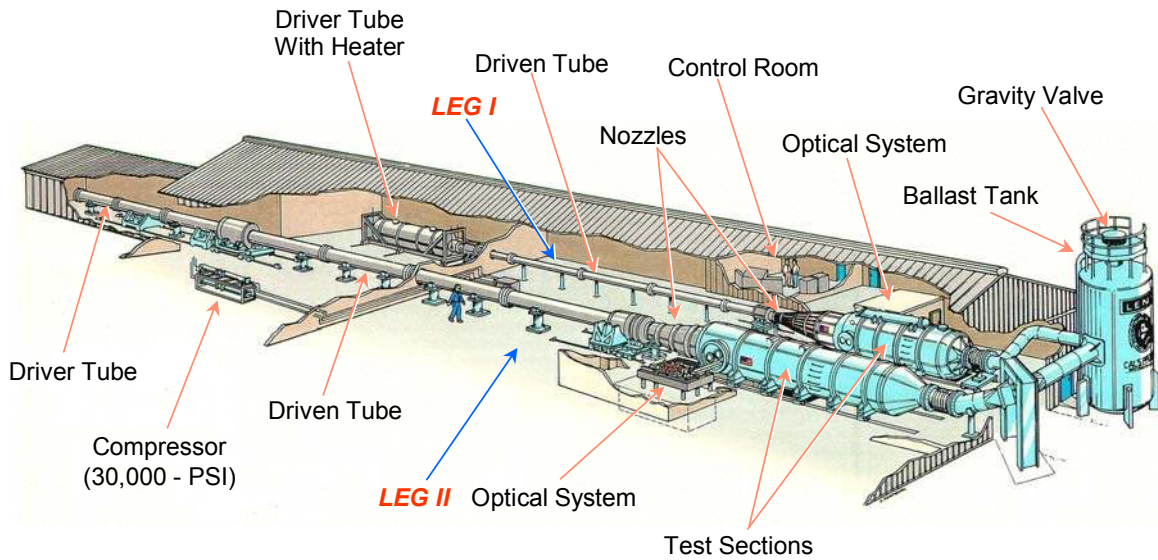


Figure 19: Schematic of Large Energy National Shock Tunnels (LENS).

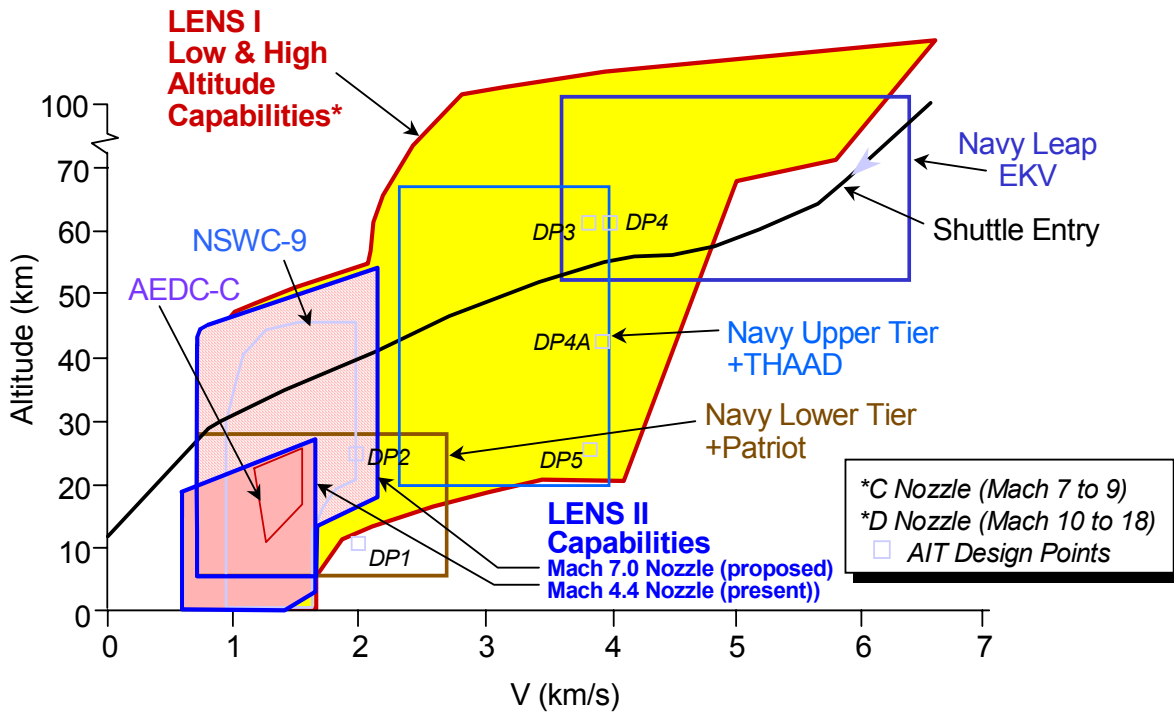


Figure 20: Velocity/Altitude Performance of the LENS I and II Test Facilities.

### 2.3.3 Measurement of Tunnel Stagnation and Freestream Conditions

The facility test conditions are established and validated by a combination of measurements in the reservoir region and test section of the tunnel. The stagnation pressure and enthalpy are obtained directly from pressure measurements in the driven tube behind the reflected shock, and measurements of the incident and reflected shock Mach number made with thin-film high frequency heat transfer gages. Conditions in the freestream are obtained from survey rakes (similar to those shown in Figure 21) containing pitot pressure, cone pressure, and static pressure probes, stagnation heat transfer probes (hemispherical and two-dimensional cylinders containing platinum thin film resistance thermometers and coaxial thermocouple gages), and total temperature measurements with vented thermocouple probes (where applicable). From these probes, we can determine the freestream dynamic pressure with an accuracy of  $\pm 5\%$ , the stagnation point heating with an accuracy of  $\pm 7\%$ , and the freestream Mach number with an accuracy of  $\pm 1.5\%$ . A typical distribution of Mach number from a flow field survey conducted just prior to the beginning of the cylinder/flare studies in LENS I is shown for the conditions in Figure 22.

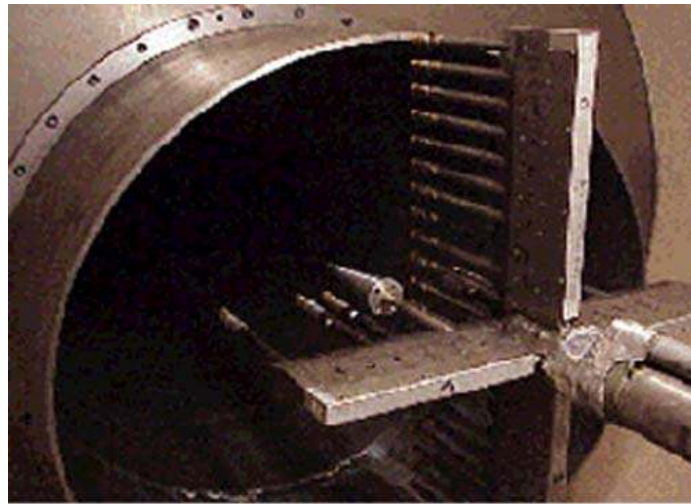


Figure 21: Rake Installed in LENS I Shock Tunnel.

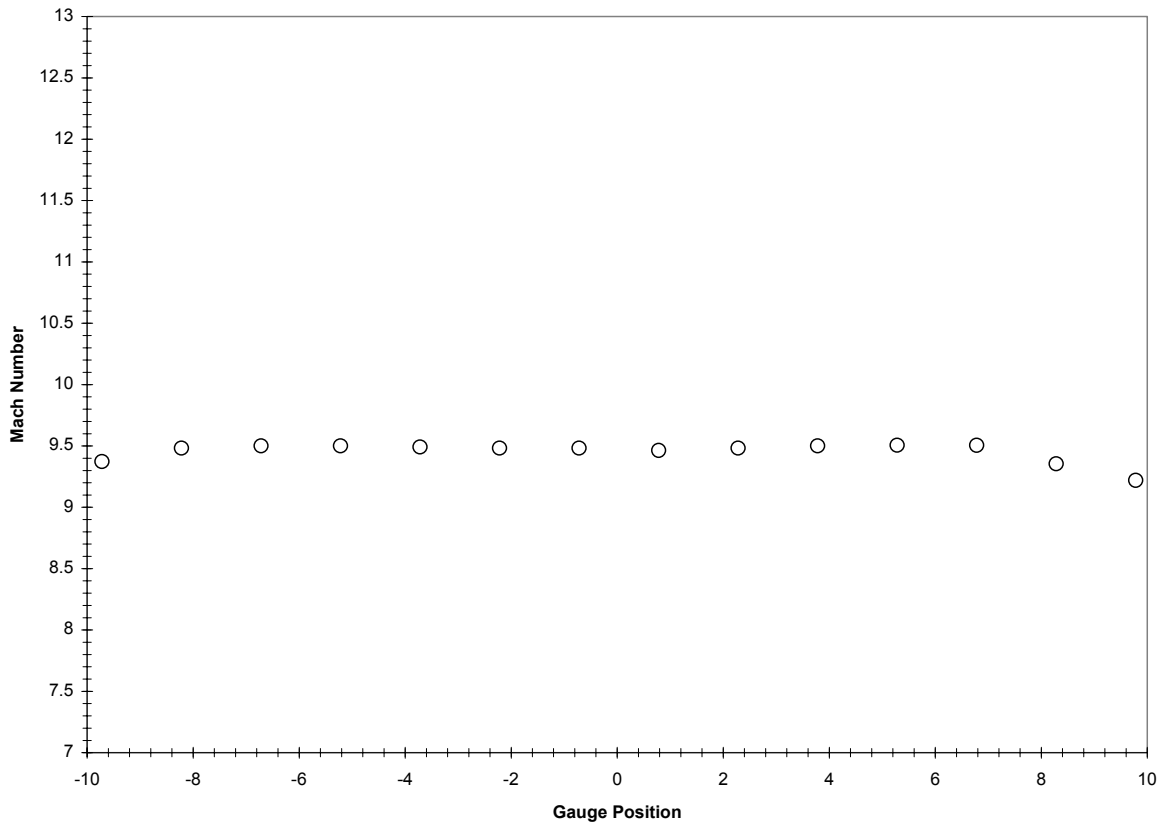


Figure 22: Mach Number Distribution across Test Core from LENS Leg I Indented Cone Tunnel Calibration Airflow – Calibration Measurements prior to the Double Cone Studies.

### 3 PRESENTATION OF EXPERIMENTAL MEASUREMENTS

#### 3.1 Measurements with the Hollow Cylinder and with the 25° Cone Model to Examine Effects of Freestream Vibrational Nonequilibrium

##### 3.1.1 Introduction

The experiments conducted in this second phase of the program were designed to provide us with a better understanding of the contribution of vibrational nonequilibrium on the properties in the freestream and on the heating and pressure levels of the model. Vibrational nonequilibrium effects have been extensively researched particularly at the Cornell Aeronautical Laboratory (CAL), predecessor of CUBRC, where the classic work of Treanor (Ref. 9) has defined the basic mechanisms involved in these flows. However, despite the relatively extensive theoretical studies there has been little direct confirmation from measurements made in wind tunnels in hypervelocity airflows. It has been generally accepted that the effects of air chemistry on the freestream properties overwhelm the vibrational nonequilibrium effects for hypersonic airflows at velocities of 9,000 ft/sec and above, where the energy exchange between vibration and the reacting components of the airflow, it is rapid enough to bring the vibrational temperature close to the translation temperature of the flow. For nitrogen flows, in a similar velocity range, the situation is somewhat different. For totally pure nitrogen



flows, for which the vibrational relaxation rates are low, the freezing of energy in the vibrational mode at or just downstream of the throat can result in a significant amount of energy locked in the flow through the test section. However, in the presence of impurities such as water vapor, there is significant debate as to whether these impurities accelerate the vibrational relaxation process in the nozzle. If the relaxation is enhanced, energy is returned to the flow in the form of increased velocity as the vibrational temperature drops towards the translational levels. Evidence to suggest this might happen has been presented by Boudreau (Ref. 10) on studies in Hotshot facilities (which in fact can contain more impurities than just water vapor) with measurements indicating that vibrational “thawing” occurs where the vibrational temperature relaxes more quickly to the translational temperature than would be predicted with the standard relaxation rates. There has been a generally held belief that in many nitrogen tunnels the vibrational temperature is closer to that of translation than the calculations suggest. However, in most hypersonic facilities, the stagnation temperature of the flow is designed to be just sufficient to prevent condensation and cluster formation in the test section. Hence, stagnation temperatures under these conditions are well below levels where there is a significant amount of energy in vibration in the reservoir. However, when true hypervelocity flows (more representative of flight conditions) are developed in a high-enthalpy facility, vibrational nonequilibrium is an important consideration. This is particularly true for high-purity shock tunnels similar to the ones used in these experimental studies. For our studies, we filled the driven tube with nitrogen from bottles containing nitrogen which was certified to be of high purity. However, for low-density flows, where the pressure in the driven tube is below an atmosphere, water vapor adsorbed on the walls of the tunnel can be drawn into the test gas, and although these amounts are extremely small, they potentially can influence the vibrational relaxation rates. In the first part of the study, we investigated the effects of the levels of water vapor in the driven tube by conducting studies where a hard vacuum was applied to the driven tube for over three days to eliminate as much water as possible, to the other extreme where water was introduced in the tube in order to saturate the flow. We compared the heat transfer measurements to the cone and cylinder for these conditions as well as for the conditions developed during a normal testing cycle where the driven tube was subjected to a vacuum for a relatively short time. Shown in Figure 23 are the heat transfer measurements made for the three levels of water vapor in the facility. It can be seen that there is virtually no difference between the measurements made for the two cases where we do not introduce water into the flow. For the case when water is added, the heating levels are indeed smaller, which almost certainly results from the energy absorbed in water vapor. For standards tests in which high purity gas is used, we believe that it is a reasonable assumption that the flows can be computed accurately using the classical rates suggested by Millikan and White (Ref. 11) for vibrational nonequilibrium. The flows in the test section for the experiments discussed below and for the test cases employed in the validation study (Ref. 5) were recomputed using our 2D nonequilibrium airflow code (NETCON) and the full Navier-Stokes computation incorporating flowfield chemistry developed by Graham Candler for the expansion down the contoured nozzle used in the experimental studies. Although different assumptions are made to describe the development of the boundary layer down the nozzle, the two sets of computations were found to be in excellent agreement with predicted differences in the freestream velocity of less than 1% (Ref. 12).

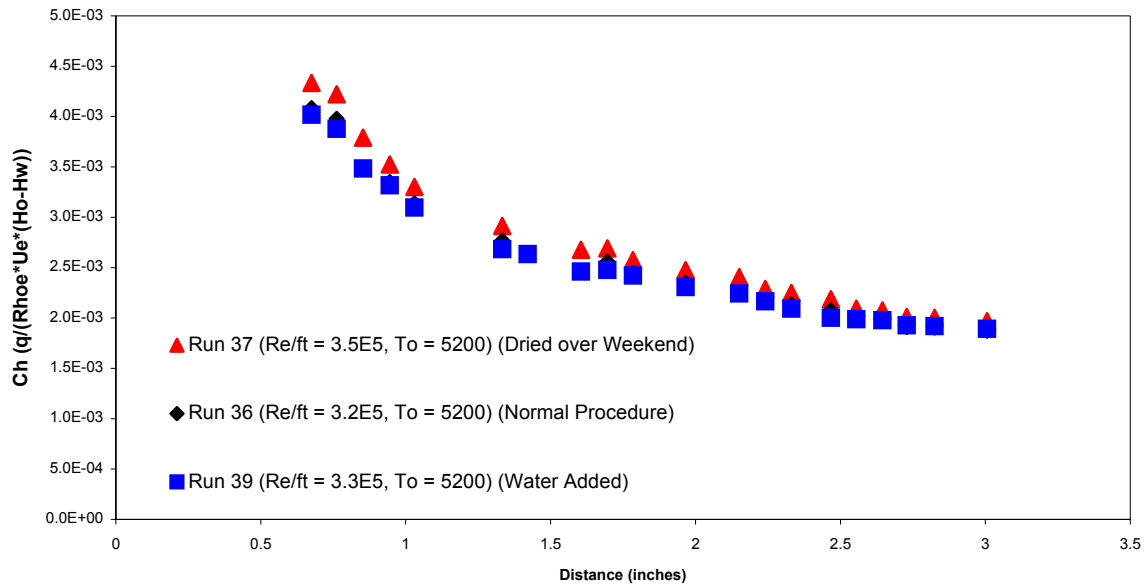


Figure 23: Results of Studies to Evaluate the Effects of Water Vapor in the Test Gas on the Heating Rates along the Cone.

### 3.1.2 Survey Rake Measurements to Define Freestream Properties

Flowfield surveys were made at each of the test conditions for which code validation measurements were made on the double cone and the hollow cylinder/flare model. The survey rake (which was similar to that shown in Figure 21) contained a full complement of pitot pressure gages as well as heat transfer instrumentation to measure the heating in the stagnation region and around the hemispherical probes. We also employed cone probes, which, in conjunction with the pitot probes, can be used to provide measurements of the static pressure in the freestream. As discussed in Section 2.3.3, the freestream properties are derived in our non-equilibrium nozzle code (Ref. 13) from measurements of the pressure and enthalpy in the tunnel reservoir and pitot pressure in the test section; the stagnation point heating and cone pressure data provides additional validation of the test conditions. Examples of the Mach number distributions across the core flow are shown in Figures 16 and 22. The model support system and survey rake assembly employed in the studies with the hollow cylinder and the 25° cone are shown in Figures 6 and 12 respectively. With the models placed in the core of the flowfield the pitot probes and supporting survey probes (see Section 2.2) were positioned to include also measurements of the structure of the outer flow and nozzle boundary layer. This information was then available to evaluate the effectiveness of the models employed by Candler (Ref. 14) to compute the turbulent boundary layer growth along the walls of the contoured “D” nozzle. Examples of the comparisons between the rake measurements and the predicted distribution of Mach number are shown in Figures 24 and 25. The good agreement shown in this figure provides strong support for the models used in the codes.

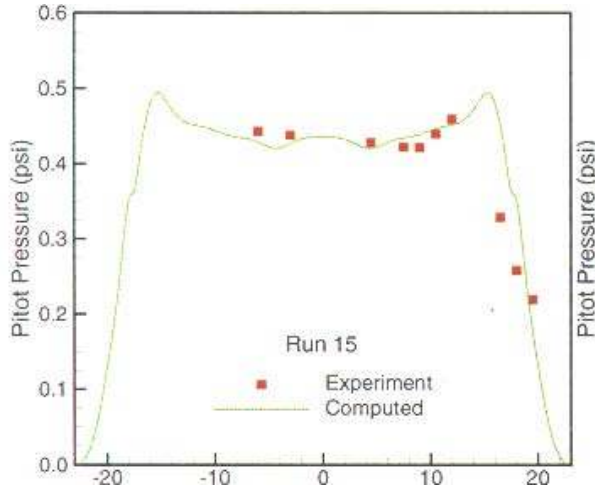


Figure 24: Comparisons between Measured and Predicted Pitot Distribution for Run 15 to Validate Model of Viscous Layer in Nozzle Code.

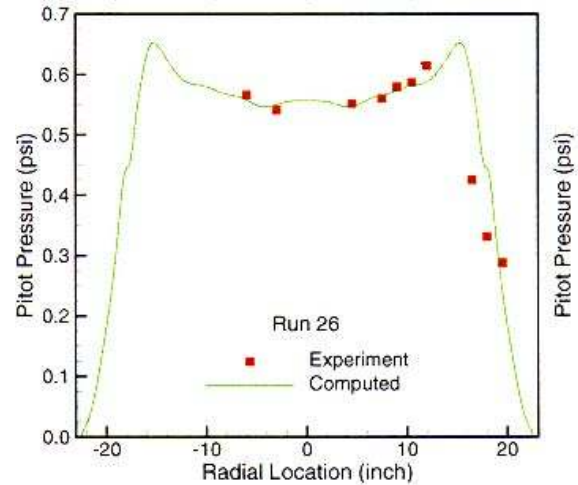


Figure 25: Comparisons between Measured and Predicted Pitot Pressure for Run 26 to Validate Model of Viscous Layer in Nozzle Code.

### 3.1.3 Studies to Examine Vibrational Nonequilibrium Effects on the Heating and Pressure Distribution to the 25° Cone

In this segment of the experimental program we made detailed measurements of heat transfer on two 25° cones and surface pressure measurements were made on one cone, for a large range of reservoir enthalpies and pressures. From this, it was possible to examine how the heating levels were influenced by the magnitude of the energy frozen in vibration in the flow through the test section. The flow conditions at which the studies were conducted are listed in Table I, which shows that the measurements were made for stagnation temperatures of 5000°R (at which the double cone studies were conducted), down to temperatures 2,000°R where nitrogen vibration is only weakly excited. Measurements were also made for a range of stagnation pressures to vary the strength of the viscous interaction at the tip of the cone.

Table I: Vibrational Nonequilibrium Studies with 25 Degree Cone/Hollow Cylinder

Run	Po	Ho	Po'	Uinf	Rhoinf	Pinf	Tinf	Tvinf	M	Re/ft
	psia	(ft/sec) <sup>2</sup>	psia	ft/sec	slugs/ft <sup>3</sup>	psia	deg. R	deg. R		
8	543	4.00E+07	0.511	8.32E+03	1.15E-06	2.49E-03	1.76E+02	4.80E+03	12.60	6.78E+04
11	1195	3.59E+07	1.002	7.95E+03	2.48E-06	4.62E-03	1.51E+02	4.25E+03	12.97	1.63E+05
12	2529	3.70E+07	2.003	8.13E+03	4.73E-06	9.18E-03	1.57E+02	3.98E+03	13.01	3.05E+05
15	453	2.59E+07	0.431	6.74E+03	1.48E-06	2.10E-03	1.15E+02	3.61E+03	12.60	1.12E+05
16	834	2.80E+07	0.733	7.01E+03	2.33E-06	3.48E-03	1.21E+02	3.75E+03	12.78	1.72E+05
25	412	3.89E+07	0.398	8.19E+03	9.26E-07	1.96E-03	1.71E+02	4.82E+03	12.55	5.51E+04
26	599	3.72E+07	0.557	8.04E+03	1.35E-06	2.65E-03	1.60E+02	4.59E+03	12.77	8.46E+04
27	802	3.90E+07	0.964	8.23E+03	2.22E-06	5.18E-03	1.89E+02	4.59E+03	12.01	1.20E+05
31	1747	3.76E+07	1.470	8.16E+03	3.45E-06	6.90E-03	1.62E+02	4.18E+03	12.87	2.17E+05
35	775	1.63E+07	0.598	5.45E+03	3.14E-06	2.66E-03	6.88E+01	2.45E+03	13.20	3.53E+05
38	907	1.79E+07	0.689	5.70E+03	3.32E-06	3.05E-03	7.46E+01	2.65E+03	13.23	3.52E+05
40	1759	2.32E+07	1.332	6.43E+03	5.03E-06	5.97E-03	9.63E+01	3.19E+03	13.15	4.44E+05
43	469	3.66E+07	0.435	7.95E+03	1.07E-06	2.11E-03	1.59E+02	4.61E+03	12.65	6.70E+04
44	3618	3.59E+07	2.830	8.03E+03	6.86E-06	1.28E-02	1.52E+02	3.76E+03	13.08	4.54E+05

The measurements were examined (i) by comparing with directly with Candler's Navier-Stokes calculations (Ref. 7), and (ii) by correlating the measurements in terms of parameters that characterize the viscous interactions close to the tip of the cone.

Three comparisons between Candler's calculations and the heat transfer measurements over the cone are presented Figures 26, 27 and 28; these correspond to reservoir temperatures of 3,000°R, 4,000°R and 5,000°R respectively. For the low enthalpy flow (Run 15) where nonequilibrium effects are small and slip effects diminish at the rear of the cone all the solutions (shown in Figure 26) are in good agreement with the measurements. From Figure 27 it can be seen that at the intermediate stagnation temperature, high-pressure condition at which Run 12 was conducted, the measured data are in good agreement with the calculations made by incorporating only the effects associated with vibrational nonequilibrium. For the high enthalpy low Reynolds number conditions for Run 8, Candler found that in order to obtain good agreement with the experiment, he must account for the effects of both vibrational nonequilibrium and surface slip. The heat transfer measurements made on the cone for the large range of test conditions were correlated in terms of heat transfer coefficient  $C_H$

$$C_H = q / (\Delta_e U_e [H_R - H_w])$$

and viscous interaction parameter

$$\bar{\chi}_L = M^3 \circ C^* / \circ Re_L$$

where  $H_R = C_p T_e + \circ P_r U^2 / 2$  and  $C^*$  is evaluated at the reference temperature  $T^* = T_0 (1 + 3T_w / T_0) / 6$ .

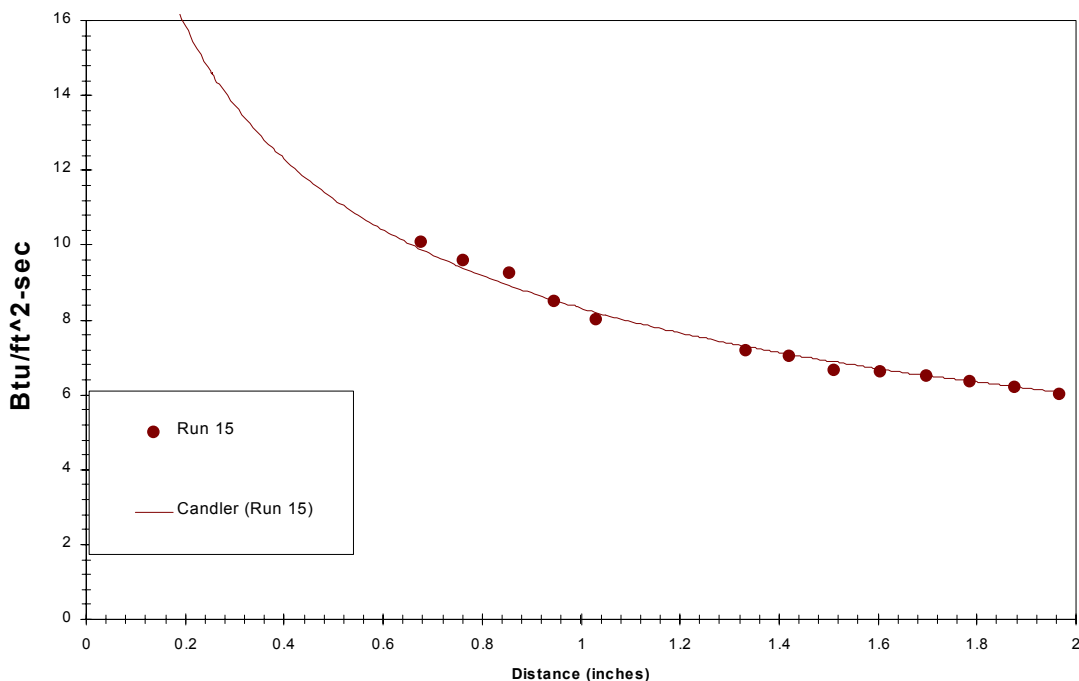


**Figure 26: Comparison between Cone Heat Transfer Measurements  
and Candler's Navier-Stokes Prediction for Run 15.**

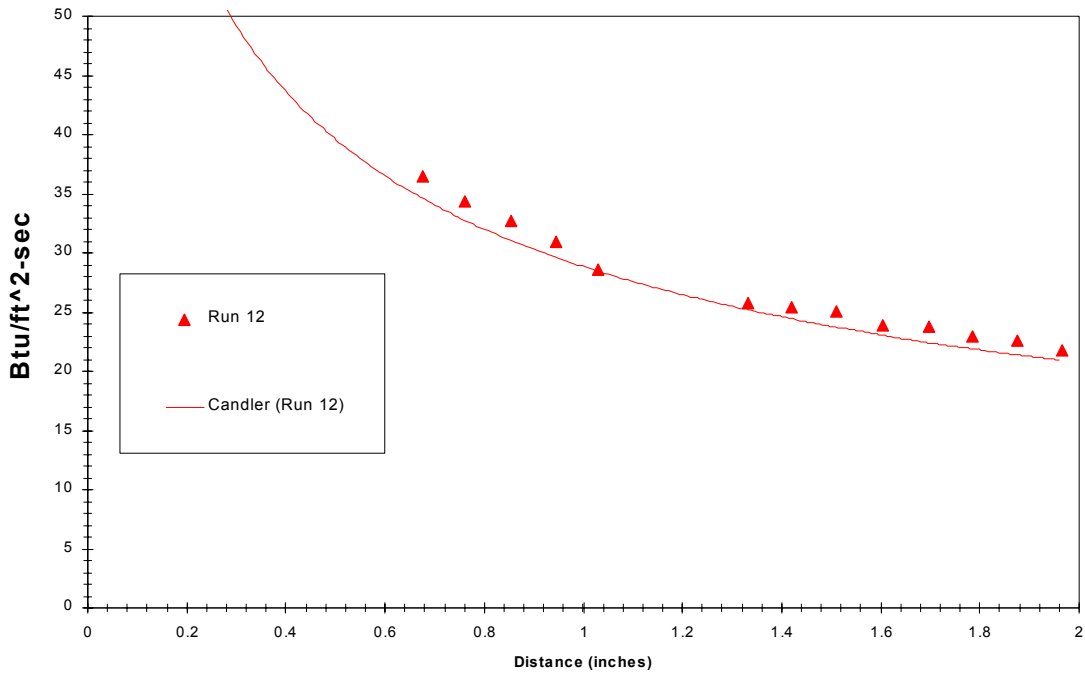


Figure 27: Comparison between Cone Heat Transfer Measurements and Candler's Navier-Stokes Prediction for Run 12.

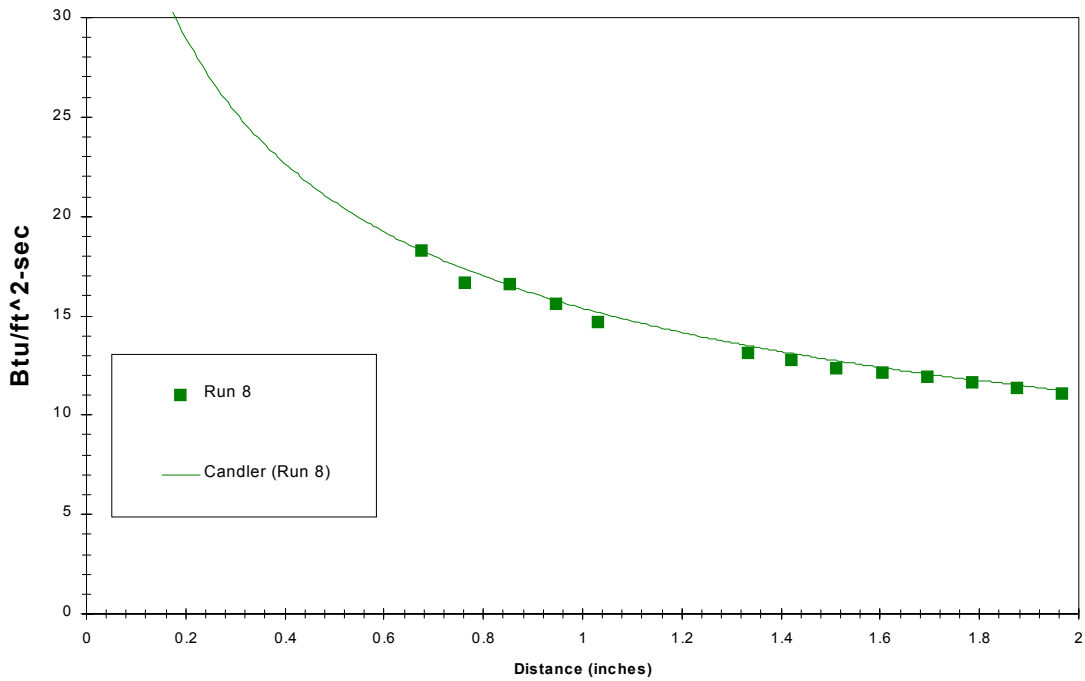
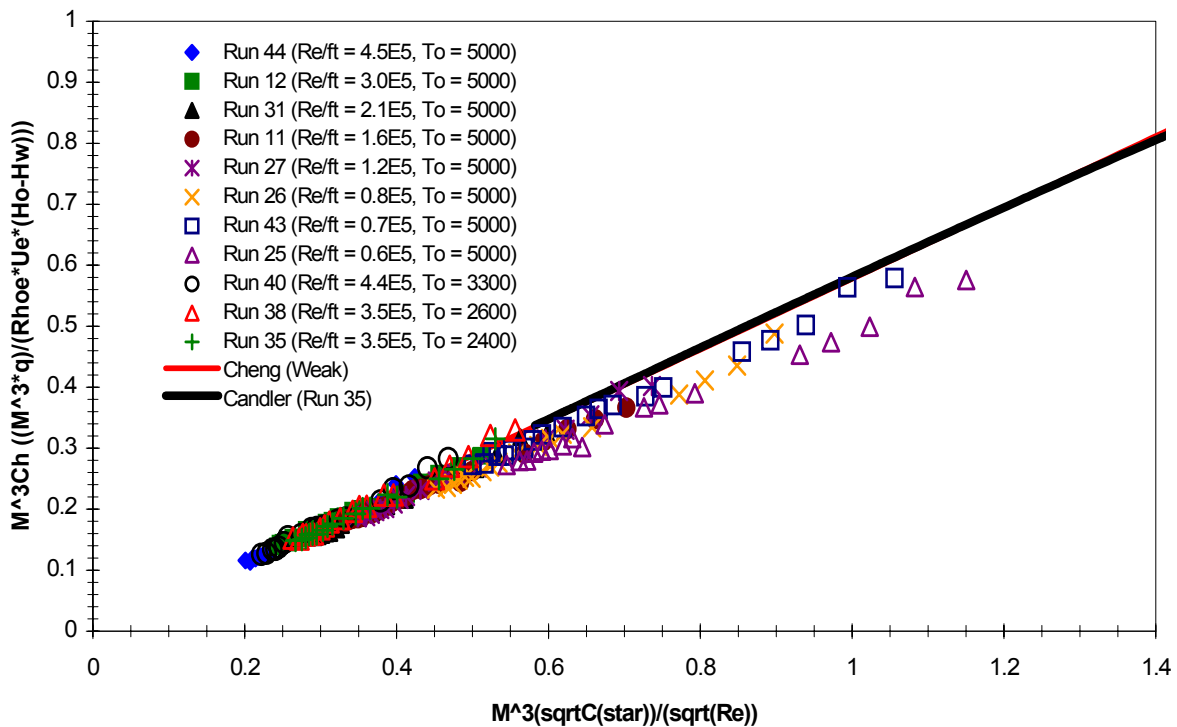


Figure 28: Comparison between Cone Heat Transfer Measurements and Candler's Navier-Stokes Prediction for Run 8.

Comparisons have been made for the range of freestream conditions listed in Table I. The sensitivity of the heat transfer coefficient to Mach number has been removed empirically by multiplying it by the cube of the Mach number. This product, plotted against  $\bar{\chi}_L$  is presented in Figure 29. Although it is difficult to see because the measurements obscure the lines, at small values of  $\bar{\chi}_L$  the measured data are in relatively good agreement with Cheng's empirical prediction methods (Ref. 16) and Candler's Navier-Stokes computations. At more rarefied conditions, the heating is less than predicted by either method. This effect is more easily observed by plotting only the measurements obtained at the highest enthalpy conditions, where, as shown in Figure 30, Candler's predictions including slip are seen to be in good agreement with the measurements, except for the data at the most rarefied values of  $\bar{\chi}_L$ . Plotting the measurements for the largest unit Reynolds number, as shown in Figure 31, we observe good agreement with the empirical methods and the Navier-Stokes predictions. Figure 32 shows a correlation of the pressure measurements and the semi-empirical and Navier-Stokes predictions. This demonstrates good agreement and is indicative of the cone pressures being only very weakly influenced by vibrational nonequilibrium.



**Figure 29: Correlation of All Cone Heating Measurements and  
Comparison with Simple Navier-Stokes Prediction Methods.**



Nondimensional Heat Transfer Cone Data ( $M^3Ch$  vs  $Chi(\bar{c})$ )  
Reynolds Number Sweep ( $T_0 = 5000$  Nominally)

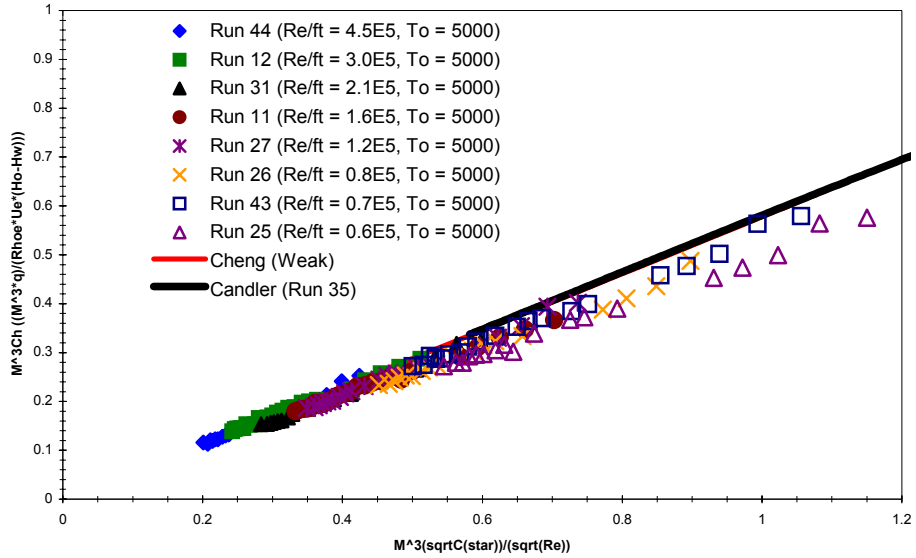


Figure 30: Correlation of Cone Heating Measurements and Comparison with Prediction Methods for High Stagnation Temperature Conditions Only.

Nondimensional Heat Transfer Cone Data ( $M^3Ch$  vs  $Chi(\bar{c})$ )  
 $T_0$  Sweep ( $Re = 3.5E5$  Nominally)

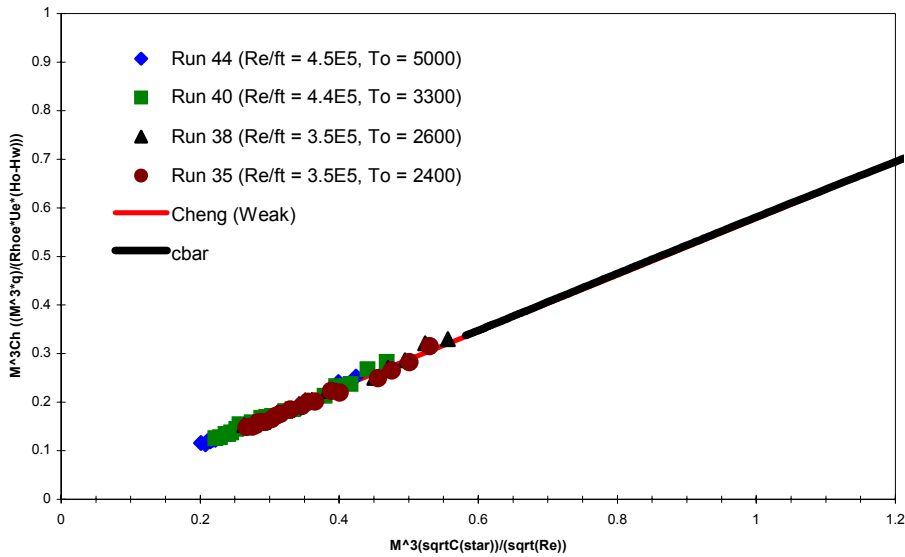


Figure 31: Correlation of Cone Heating Measurements and Comparison with Prediction Measurements for High Reynolds Number Conditions Only.

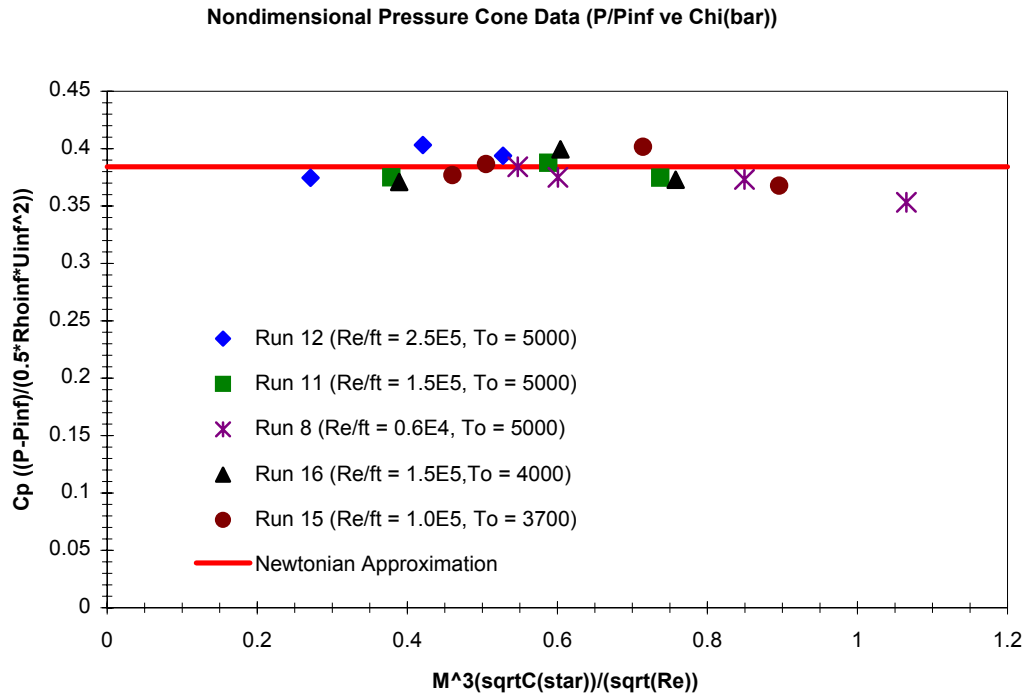


Figure 32: Comparison of Measurement of Cone Pressure and Predictions from Newtonian and Navier-Stokes Codes.

### 3.1.4 Examination of Effects of Reservoir Pressure and Enthalpy on the Pressure and Heating on the Hollow Cylinder Model

The studies with the hollow cylinder followed the cone study; however in this segment of the program, we also obtained measurements on one of the cone models positioned on the rake as shown in Figure 6. Measurements of heat transfer and surface pressure distributions were again made for a large range of reservoir enthalpies and pressures, (see Table I) to examine how the heating and pressure levels were influenced by the energy frozen in vibration in the flow through the test section, and to vary the characteristics of the viscous interaction over the leading edge of the cylinder.

Again we compared our measurements with Candler's computations, correlating them in terms of similarity parameters. Comparisons between experiment and predictions for Runs 26 and 43 are shown in Figures 33 and 34 respectively. Both have similar free stream velocities but Run 26 was conducted at a larger reservoir pressure. In this latter case the slip effects are smaller and this is reflected in the calculations. However, to predict the data for Run 43 most accurately, nonequilibrium vibration and slip must both be included in the calculation. We again correlated the heat transfer and pressure measurements to the cylinder in terms of the same heat transfer and viscous interaction parameters used for the cone measurements. Figure 35 shows the result for all the heat transfer measurements on the hollow cylinder together with semi-empirical and Navier-Stokes predictions. At large values of  $\bar{\chi}_L$  we again see evidence of decreased heating resulting from slip effects. This is more easily observed by plotting the measurements taken at the highest enthalpy condition for a range of Reynolds numbers as shown in Figure 36. Finally, we see that (as shown in Figure 37)

the measurements are in good agreement with predictions at the highest Reynolds number conditions. Figure 38 shows the correlation of pressure over the cylinder flare model. Here we see that the weak interaction theory is in relatively good agreement with the measurements as are the predictions of Candler.

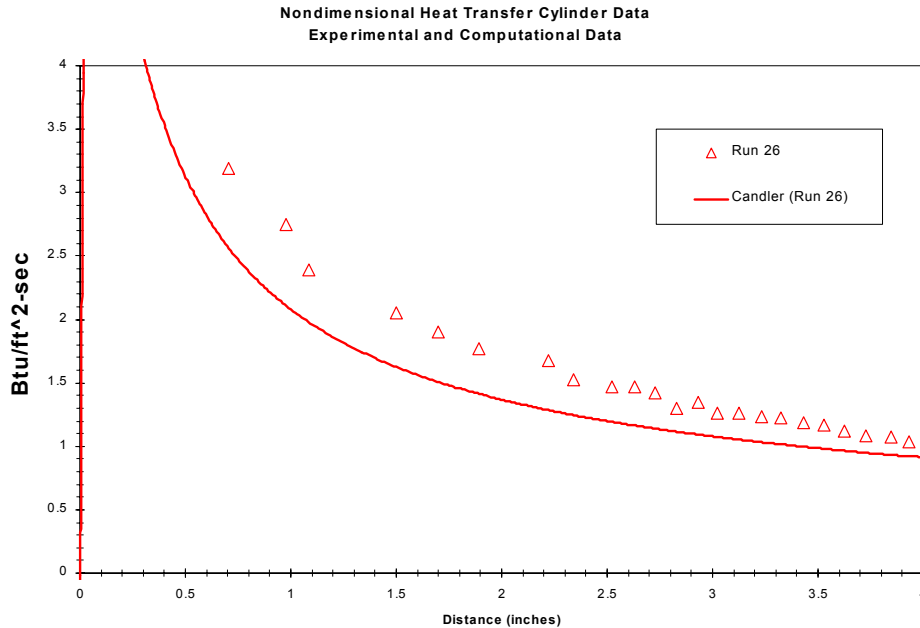


Figure 33: Comparison of Measurements of Heat Transfer on Cylinder and Candler's Predictions with Slip for Run 26.

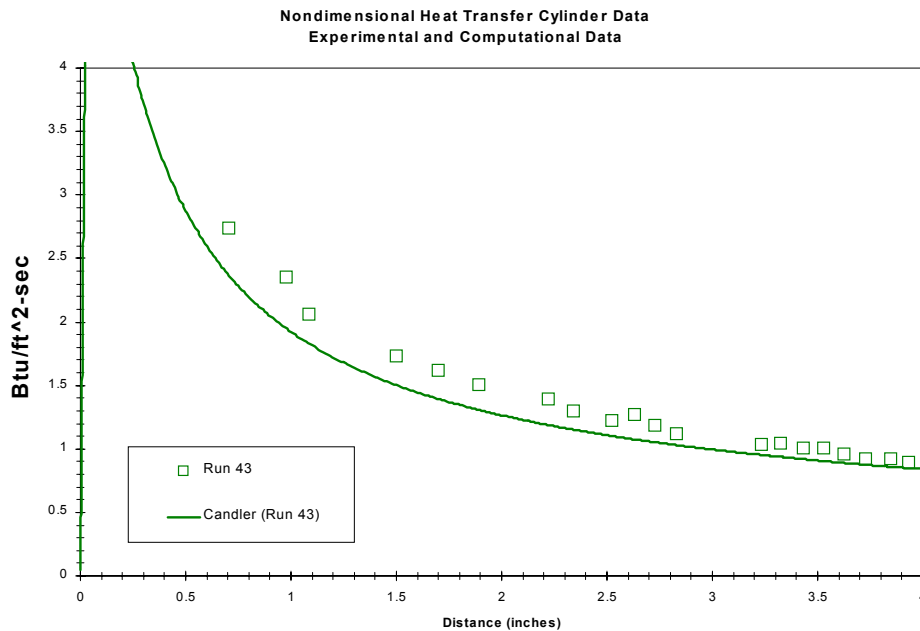


Figure 34: Comparison of Measurements of Heat Transfer on Cylinder and Candler's Predictions with Slip for Run 43.

Nondimensional Heat Transfer Cylinder Data ( $M^3Ch$  vs  $Chi(\text{bar})$ )

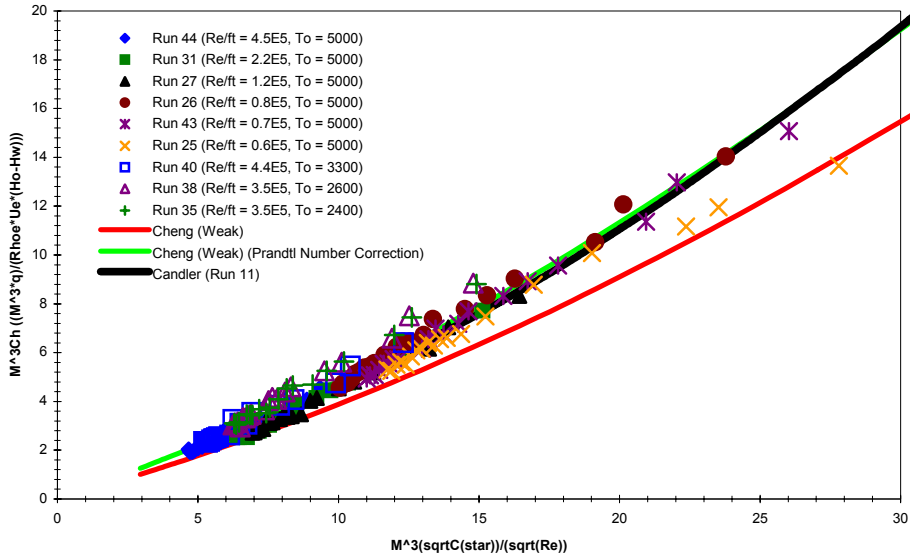


Figure 35: Correlation of All Cylinder Measurements and Comparison with Simple and Navier-Stokes Prediction Methods.

Nondimensional Heat Transfer Cylinder Data ( $M^3Ch$  vs  $Chi(\text{bar})$ )  
Reynolds Number Sweep ( $T_0 = 5000$  Nominally)

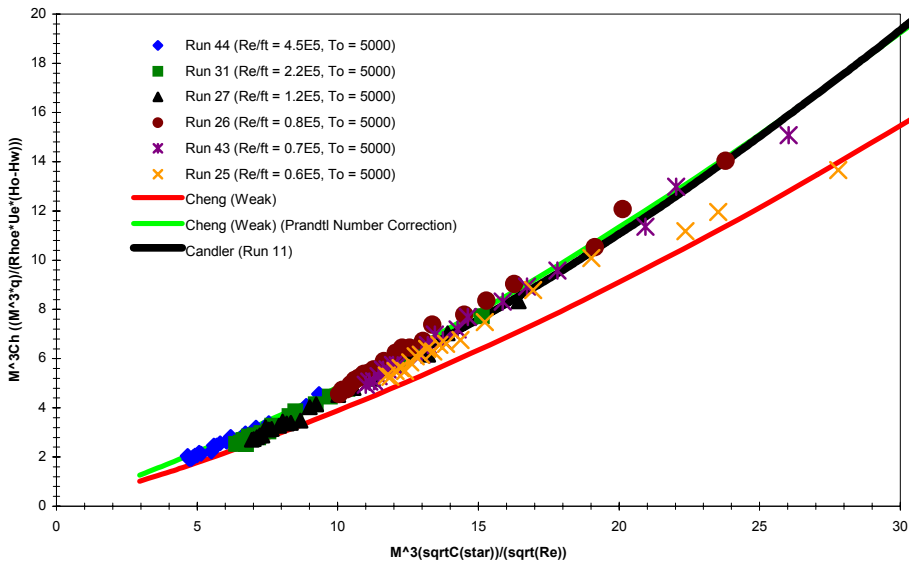


Figure 36: Correlation of Cylinder Heating and Comparison with Simple and Navier-Stokes Predictions.

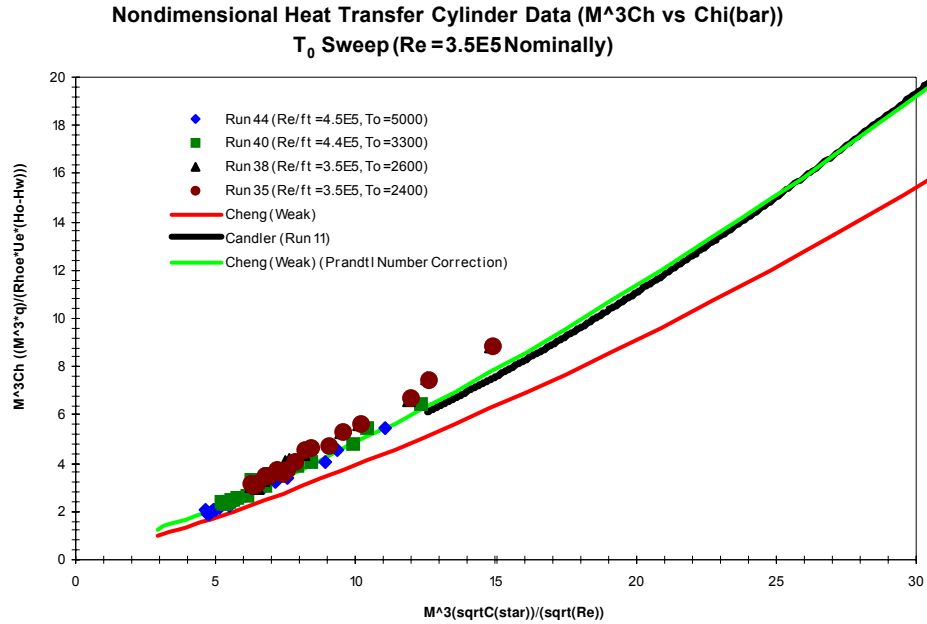


Figure 37: Correlation of Cylinder Heating and Comparison with Predictions for Only High-Temperature Flows.

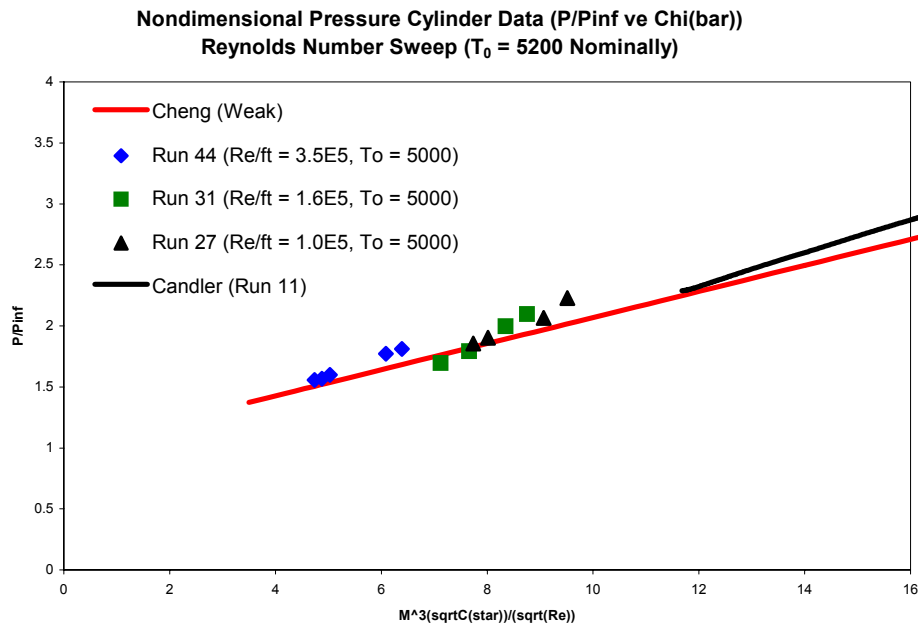


Figure 38: Correlation of Cylinder Heating Measurements and Comparison with Prediction Methods for High Reynolds Number Data Only.

## 3.2 Measurements on the Double Cone Models and Comparison with Predictions

### 3.2.1 Introduction

The studies with the double cone configuration were initially conducted as part of an investigation sponsored by AFOSR to examine and model real-gas effects in hypersonic flows. During the course of these studies, researchers at Calspan-University at Buffalo Research Center (CUBRC) and Cal-Tech decided that one approach to evaluating the models of air thermal nonequilibrium and chemistry employed in the Navier-Stokes prediction techniques was to perform experiments with model configurations the flows over which were calculated to be sensitive to real-gas effects. The studies performed at Cal-Tech concentrated on a double wedge configuration, while those employed in the experiments at CUBRC employed an “indented nose” or double cone configurations similar to those investigated earlier in studies of idealized ablated nose shapes. The flowfields over these configurations involved both separated regions induced by shock/boundary layer interaction and regions of shock/shock interaction resulting from the intersection of the forebody shock with the shock generated by the second compression surface. Calculations by Candler showed that these flows were extremely sensitive to the models of air thermal nonequilibrium and chemistry employed in the calculations.

On the basis of earlier indented nose studies, we selected a  $25^\circ/60^\circ$  double cone configuration for our initial studies. Measurements were made in both air and nitrogen flows, and these studies indicated that there were significant real gas effects on the size and properties of the interaction regions (Holden, Ref. 4). However, the flowfield configurations coupled with limited instrumentation did not allow us to draw a conclusion that the flow remained fully laminar throughout the interaction region, and therefore, these experiments did not meet the requirements of a study with well-defined boundary conditions with the avoidance of uncertainties that arise due to transition somewhere within the flow. In addition, first Candler and then Gnoffo found that they could not obtain stable flowfields over these configurations, suggesting that the flow may be intrinsically unsteady or that the differencing schemes were unsuitable for these flow configurations. Based on this experience, we decided to build a new series of models with significantly more instrumentation and to conduct experiments for conditions where the flows would remain laminar over the complete model and well-defined regions of attached flow were generated both upstream and downstream of the shock/boundary layer and shock/shock interaction regions.

The run matrix for the studies on the double cone configurations is listed in Table II (care should be exercised in referencing the run numbers in this table as in some instances they duplicate those shown for the sequences in Tables I and III). Although the major studies were conducted with a  $25^\circ/55^\circ$  configuration, we began our studies with the  $25^\circ/60^\circ$  double cone configuration to examine in more detail whether these flows were unstable, as implied by the numerical codes. Measurements were made for a range of freestream conditions and nosetip bluntnesses with these configurations being selected so that well-defined attached laminar boundary layers were obtained both upstream and downstream of the interaction regions. We then selected tests from this series conducted in the 48-inch tunnel and repeated these in the LENS I facility to establish facility-to-facility validation of the measurements. Studies were also conducted in the LENS I facility with fast-response temperature sensitive paint to confirm the axisymmetric nature of the flow over the body. The facility validation studies as well as those conducted with  $25^\circ/60^\circ$  double cone configuration are discussed in Reference 5. Only details of the tests on the  $25^\circ/55^\circ$  cone are included in this paper.



Table II: Cone/Cone Test Conditions

Run	Po	Ho	Po'	Uinf	Rhoinf	Pinf	Tinf	Tvinf	M	Re/ft	Nose	Cone/Flare
	psia	(ft/sec) <sup>2</sup>	psia	ft/sec	slugs/ft <sup>3</sup>	psia	deg. R	deg. R				
24	531	4.26E+07	1.25	8.57E+03	2.66E-06	8.98E-03	2.74E+02	4.75E+03	10.38	1.04E+05	Sharp	25° /55°
26	407	4.19E+07	0.975	8.47E+03	2.12E-06	7.06E-03	2.70E+02	4.86E+03	10.34	8.35E+04	Sharp	25° /55°
28	275	4.02E+07	0.619	8.27E+03	1.41E-06	4.35E-03	2.50E+02	4.93E+03	10.50	5.83E+04	Sharp	25° /55°
35	547	4.12E+07	0.541	8.45E+03	1.18E-06	2.69E-03	1.84E+02	4.88E+03	12.49	6.74E+04	Sharp	25° /55°
31	526	4.27E+07	0.521	8.60E+03	1.10E-06	2.62E-03	1.93E+02	4.99E+03	12.43	6.08E+04	0.25" Radius	25° /55°
32	298	4.18E+07	0.669	8.44E+03	1.47E-06	4.65E-03	2.57E+02	5.00E+03	10.56	6.01E+04	0.25" Radius	25° /55°
33	512	4.34E+07	1.2	8.65E+03	2.50E-06	8.67E-03	2.81E+02	4.79E+03	10.35	9.71E+04	0.25" Radius	25° /55°
36	415	4.20E+07	0.993	8.48E+03	2.15E-06	7.19E-03	2.70E+02	4.86E+03	10.34	8.48E+04	0.25" Radius	25° /55°
37	415	4.14E+07	0.995	8.42E+03	2.19E-06	7.19E-03	2.67E+02	4.82E+03	10.35	8.67E+04	0.288" Radius	25° /55°
38	409	3.76E+07	0.405	8.05E+03	9.76E-07	2.02E-03	1.68E+02	4.73E+03	12.47	5.83E+04	0.288" Radius	25° /55°
6	251	4.00E+07	0.565	8.24E+03	1.30E-06	3.97E-03	2.48E+02	4.95E+03	10.50	5.39E+04	0.6" Radius	25° /55°
39	526	4.07E+07	0.52	8.39E+03	1.15E-06	2.58E-03	1.82E+02	4.86E+03	12.50	6.61E+04	Sharp	25° /60°
40	522	4.18E+07	0.514	8.51E+03	1.12E-06	2.57E-03	1.87E+02	4.93E+03	12.48	6.30E+04	0.25" Radius	25° /60°

### 3.2.2 Measurements with the 25°/55° Double Cone Configuration and Comparisons with Predictions

#### Introduction

In this experimental series, we obtained measurements first with a sharp nosetip for a single condition at Mach 12 and then for a series of Reynolds numbers at Mach 10. These studies were followed by a similar series with the 0.25"-nose radius. Finally, we obtained measurements at the lowest Reynolds numbers with nose radii of 0.29" and 0.6". From the measurements made in this segment of the program, we selected four specific flow configurations for comparison with numerical predictions. The cases chosen were ones where the flow well upstream and downstream of the interaction regions exhibited well-defined regions of constant pressure.

#### Comparison with Measurements for Run 35

The first set of such measurements (Run 35) for a Mach number of 12.50 and a Reynolds number of  $6.7 \times 10^4$  is shown in Figures 39 and 40. Figure 39 shows a comparison between the experimental measurements and Candler's Navier-Stokes-based computations given in References 7 and 9. Both predictions describe the pressure and heat transfer distribution through the separated and shock/shock interaction regions with remarkable accuracy. The computed values of heating rate ahead of the separation are, however, consistently a little below the measurements. By incorporating the effects of vibrational nonequilibrium and vibrational slip, Candler's predictions for the forebody heating and length of the interaction region are slightly improved.

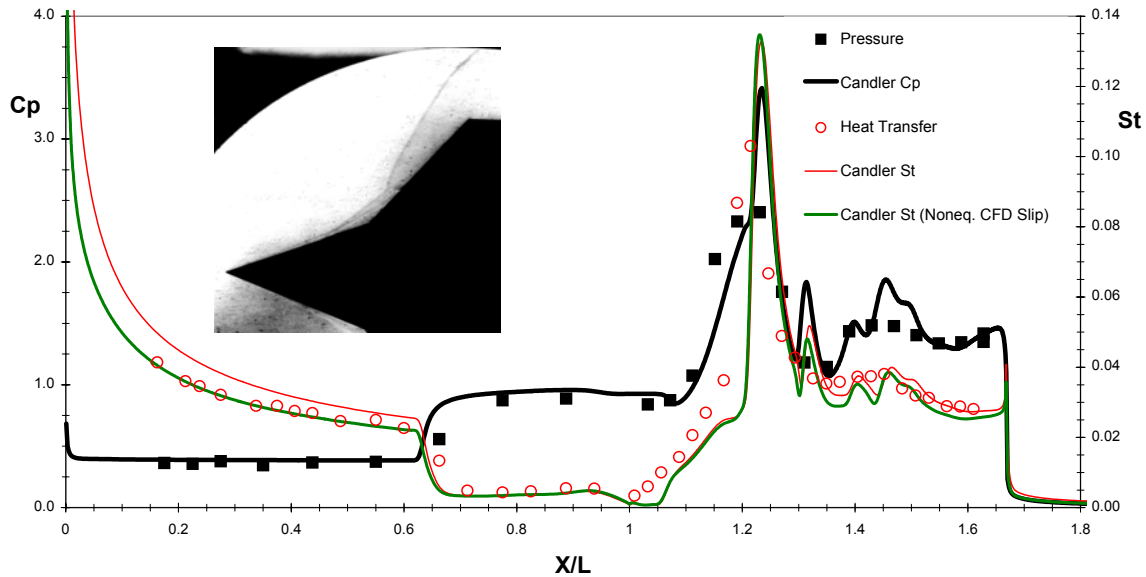


Figure 39: Candler's Predictions of Pressure, Heat Transfer and Schlieren Photograph. For Run 35 ( $M = 12.5$ ,  $Re_{\#}/ft = 6.74E+04$ ).

Boyd's predictions with the DSMC code for Run 35 are shown in Figure 40. These predictions clearly underestimate the length of the separated region and although the heating to the forebody is slightly underpredicted, there is good agreement between theory and experiment for the pressures and the heat transfer downstream of the shock/shock interaction on the second cone.

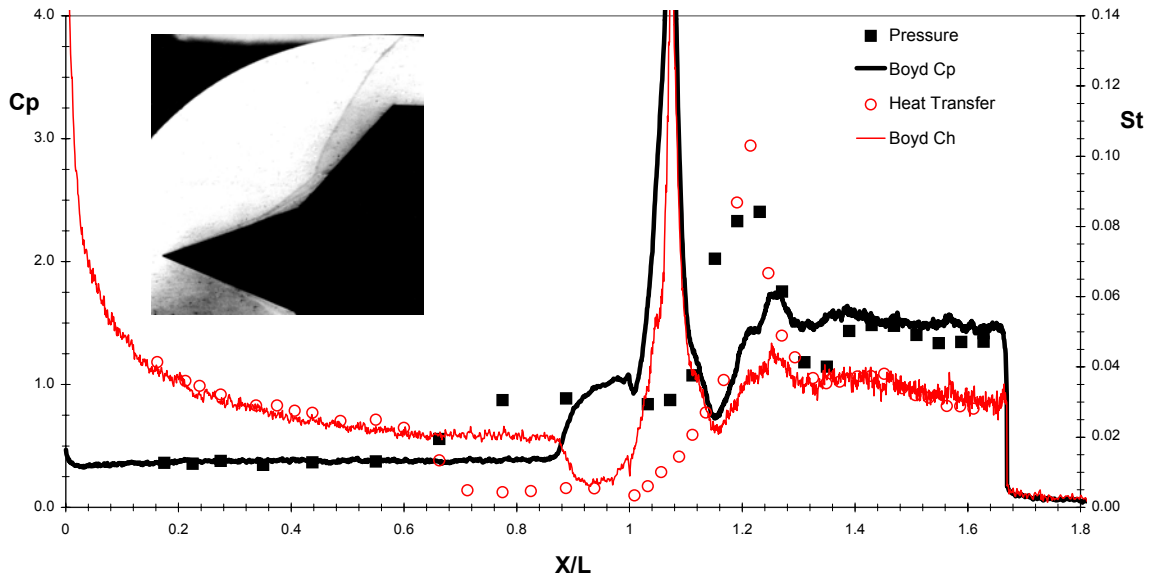


Figure 40: Pressure, Heat Transfer and Schlieren Photo.  
Run 35 ( $M = 12.5$ ,  $Re_{\#}/ft = 6.74E+04$ ) : Boyd.

*Comparison with Measurements for Run 28*

The measurements at Mach 10.5 at a similar Reynolds number of  $5.8 \times 10^4$  are compared with numerical predictions by Candler (Ref. 14), Gaitonde, and Gnoffo (Refs. 17-18) using Navier-Stokes code (Figures 41, 42, 43 respectively), and by Moss (Ref. 19) and Boyd (Ref. 15) (Figures 44 and 45) using DSMC code. For the solutions obtained by Candler, again we observe (Figure 41) excellent agreement between the predictions and experimental data for both the theoretical predictions. Adding vibrational nonequilibrium improved forebody heating prediction without changing the size and properties in the recirculation and reattachment regions.

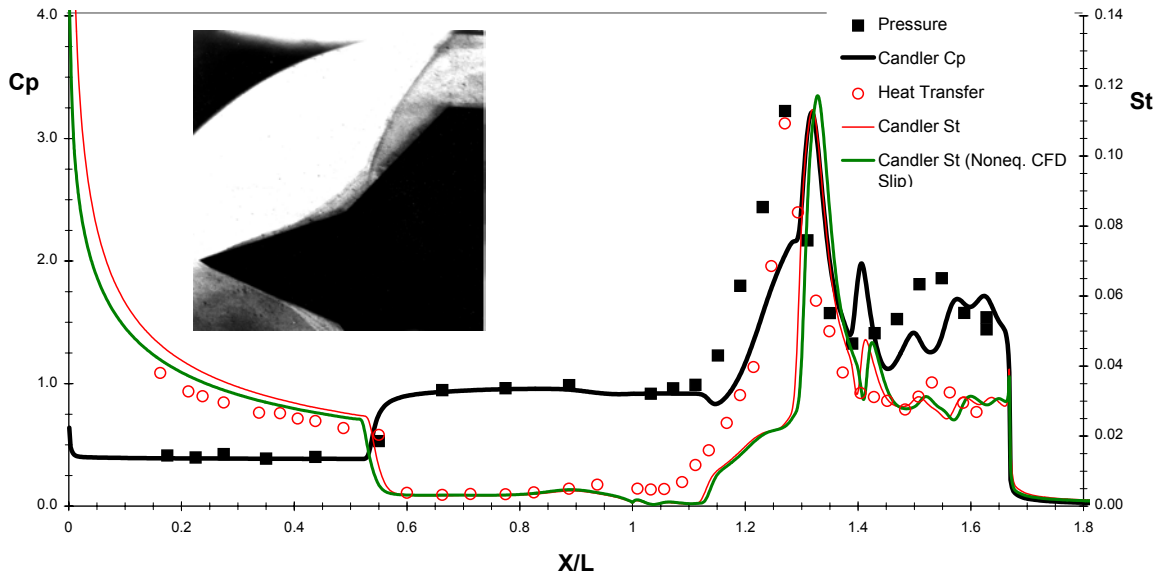


Figure 41: Pressure, Heat Transfer and Schlieren Photo.  
Run 28 ( $M = 10.49$ ,  $Re\#/ft = 5.83E+04$ ) : Candler.

The solutions obtained by Gaitonde for Run 28 (Figure 42) are in close agreement with Candler's earlier computations, giving excellent predictions of the length of the separated region and the heating in and downstream of the region of shock/shock interaction on the second cone. Adding vibrational nonequilibrium effects should improve the heat transfer predictions on the forebody.

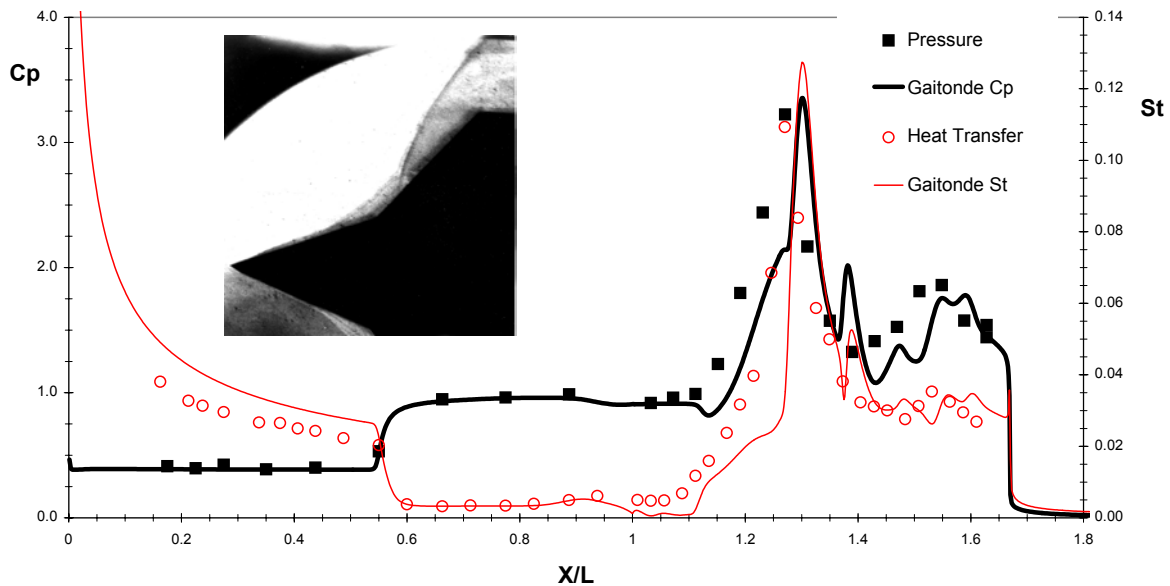
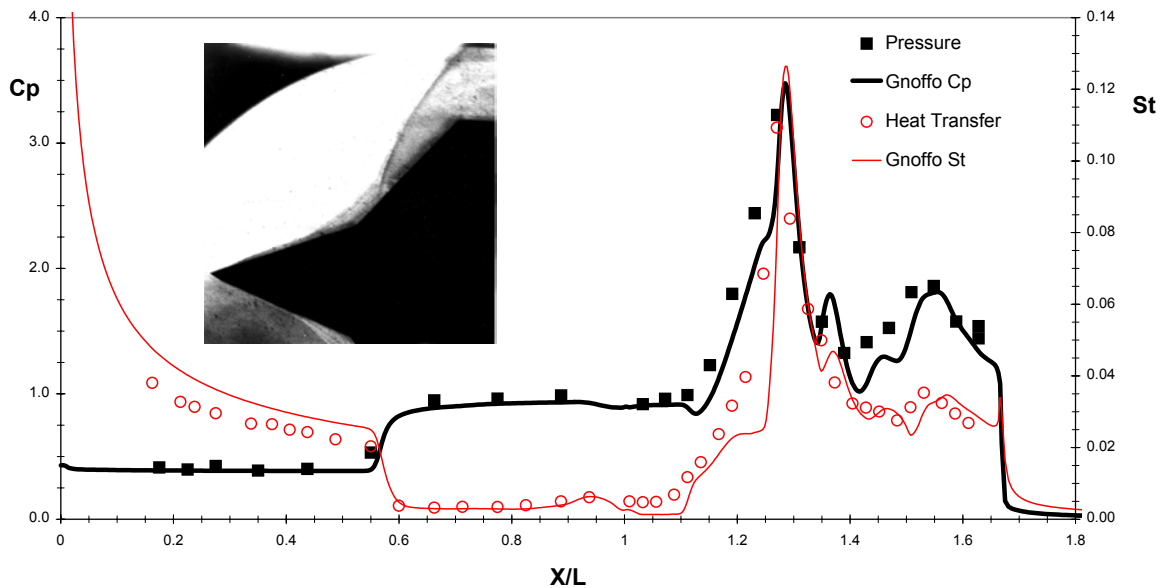


Figure 42: Pressure, Heat Transfer and Schlieren Photo.  
Run 28 ( $M = 10.49$ ,  $Re\#/ft = 5.83E+04$ ) : Gaitonde.

Similar comments can be made for the solutions of Gnoffo for Run 28 (Figure 43). Again the agreement between the theory and experiment and the different computational schemes is remarkable in the complex flows in the regions of shock/shock interaction. These calculations come the closest to predicting the exact length of separated region and the heating and pressure in the reattachment region.



**Figure 43: Pressure, Heat Transfer and Schlieren Photo.  
Run 28 ( $M = 10.49$ ,  $Re_{\#}/ft = 5.83E+04$ ) : Gnoffo.**

The next two solutions, which were obtained with the DSMC method, again significantly underpredict the scale of the interaction region and the position and magnitude of the properties in and downstream of the region of shock/shock interaction. Moss's calculations shown in Figure 44 indicate that the predicted separated region is approximately 25% of the length measured in the experiment. Downstream of the interaction regions the pressure and the heating levels are relatively well predicted. Boyd's solution for Run 28 also significantly underpredicts the length of the separated region, and unlike Moss's calculation, the heat transfer rates both ahead and downstream of the interaction and underpredicted. It is doubtful if incorporating vibrational nonequilibrium effects would significantly improve these calculations.

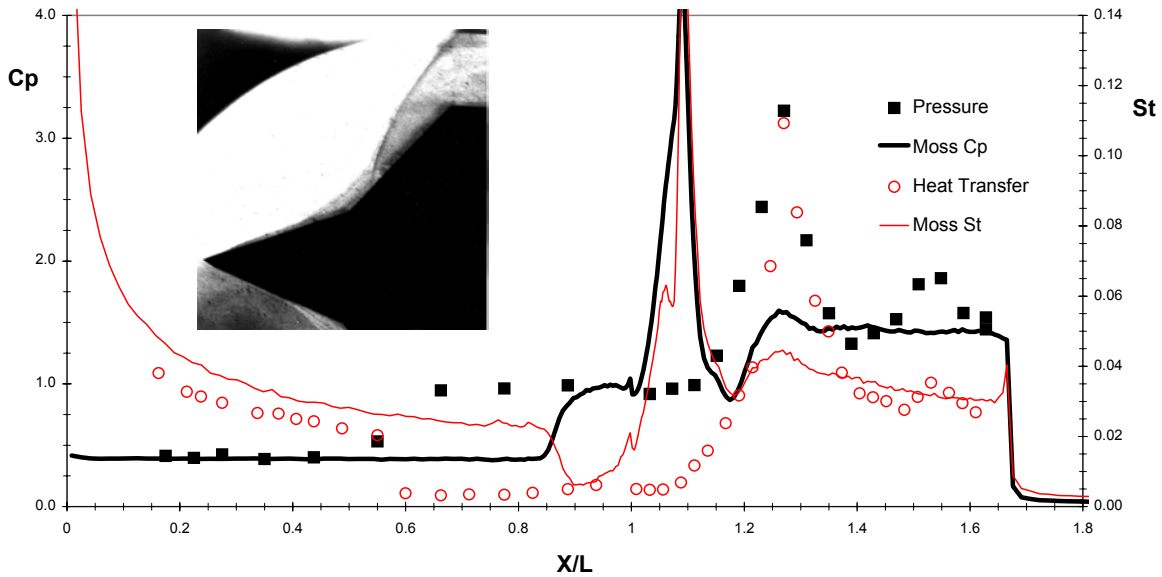


Figure 44: Pressure, Heat Transfer and Schlieren Photo.  
Run 28 ( $M = 10.49$ ,  $Re\#/ft = 5.83E+04$ ) : Moss.

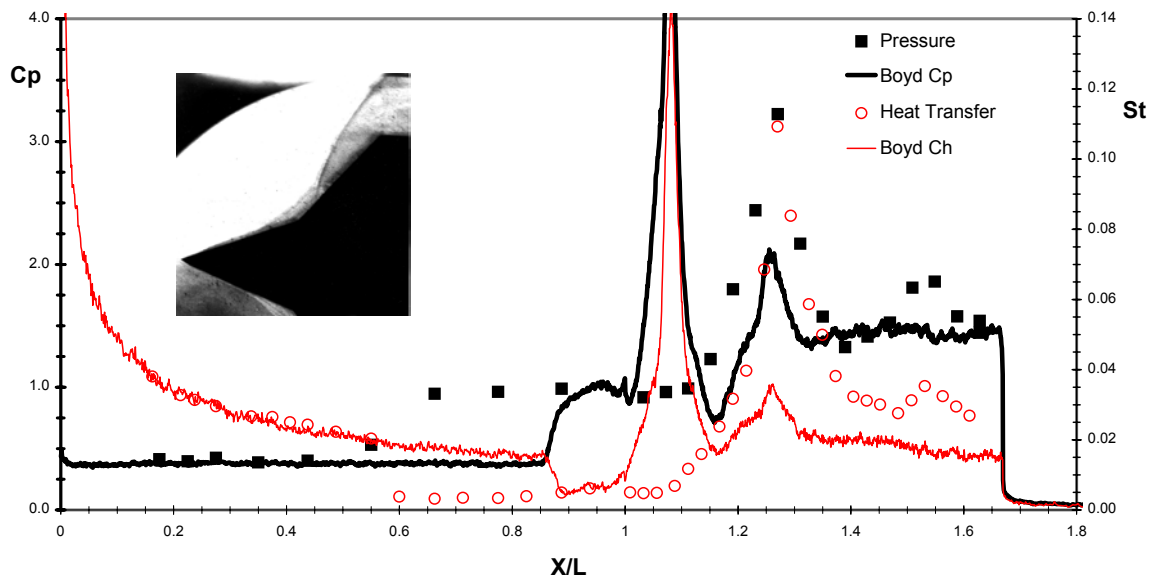


Figure 45: Pressure, Heat Transfer and Schlieren Photo.  
Run 28 ( $M = 10.49$ ,  $Re\#/ft = 5.83E+04$ ) : Boyd.

*Comparisons with Measurements for Run 31*

Predictions for Run 31 (a Mach number of 12.4 and a Reynolds number of  $6.1 \times 10^4$ ) were made by Roy (Ref. 20) using the Navier-Stokes solver, and Gallis and Bartel (Ref. 21) using the DSMC method.



The measurements for this case were made for a blunted cone with a 0.5” nose radius. Roy’s solution which is compared with the measurements of heat transfer and pressure in Figure 46 are in excellent agreement with the size and properties of the separated region, and the flow in and downstream of the reattachment compression process. The pressure distribution over the entire model is predicted almost exactly. We anticipate that the differences between the measurements and prediction would be improved by incorporating vibrational nonequilibrium effects, as they pointed out earlier. The DSMC solution by Gallis and Bartel for Run 31 again illustrates that the DSMC method significantly underpredicts the size of the separated region (see Figure 47). However, the predicted pressure levels upstream and downstream of the interaction region are in good agreement with the experiment. The heating levels throughout the interaction region are generally overpredicted. The lack of agreement between the predicted and measured separated length is surprising, since these DSMC solutions were performed with an extremely powerful computer, giving a highly resolved and converged solution.

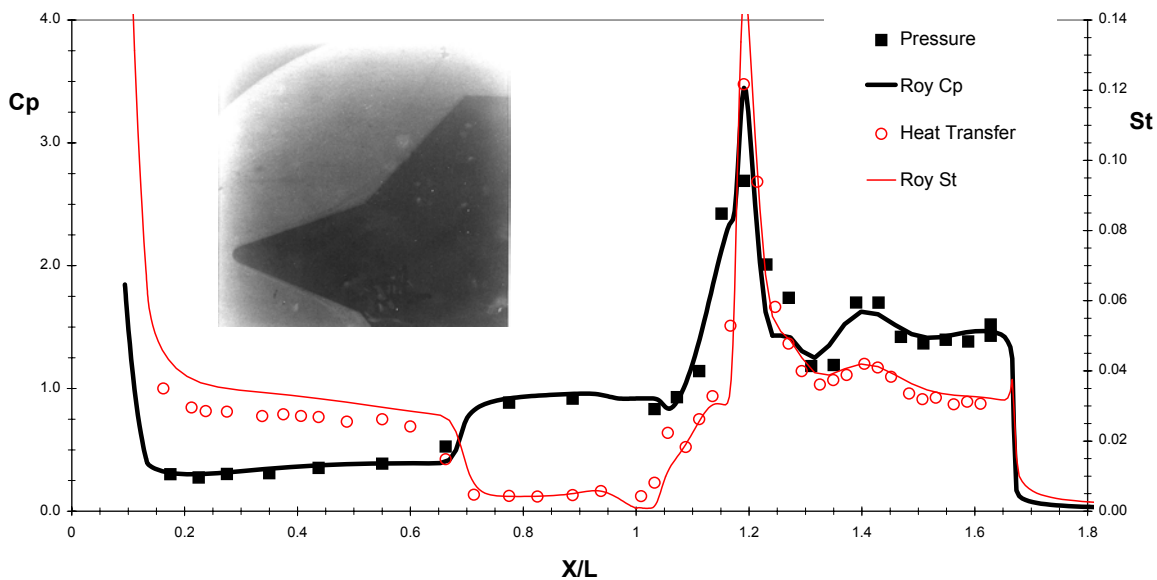
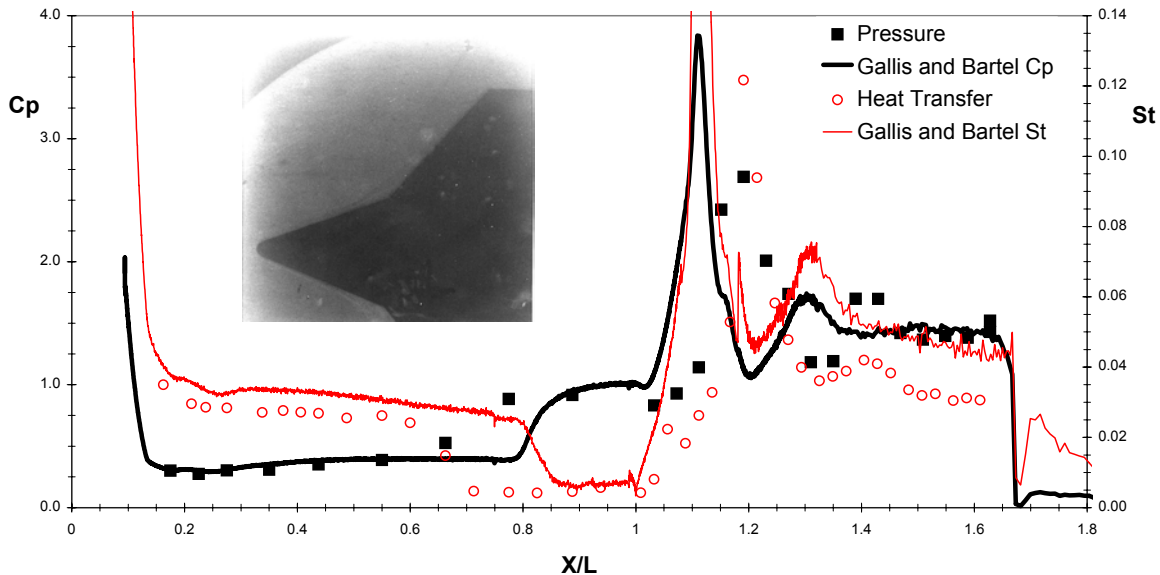


Figure 46: Pressure, Heat Transfer and Schlieren Photo.  
Run 31 ( $M = 12.4$ ,  $Re_{\#}/ft = 6.08E+04$ ) : Roy.



**Figure 47: Pressure, Heat Transfer and Schlieren Photo.  
Run 31 ( $M = 12.4$ ,  $Re_{\#}/ft = 6.08E+04$ ) : Gallis and Bartel.**

The reason for the trend seen in all of the DSMC computations to underpredict the separation length should be the focus of further study. The Gallis and Bartel computations in particular appear to be highly resolved and fully converged. The DSMC solutions advances in real time from an impulsive start, and it is possible that, although an apparent quasi-steady state has been established, insufficient time is allowed for the recirculating flow in the bubble to reach a final solution. The quasi-steady state could be established through the transmission of acoustic velocity perturbations within the solution, whereas the real flow will evolve also through a mechanism involving the transportation of fluid around the separation bubble. This process is likely to be slower and may not have been captured correctly in the DSMC solutions.

#### *Comparison with Measurements of Run 24*

Finally we compare the measurements in Run 24 at a Mach number of 10.4 and a Reynolds number of  $10.4 \times 10^4$  with solutions obtained by Gnoffo (Ref. 18) using the Laura Navier-Stokes code (Figure 48). Although the solutions slightly overpredict the length of the separated region, the pressure levels through the entire interaction region are well predicted, as are the heating levels in the separated and reattachment regions. Again, incorporating vibrational nonequilibrium into the solution could lead to more accurate predictions of the forebody heating.

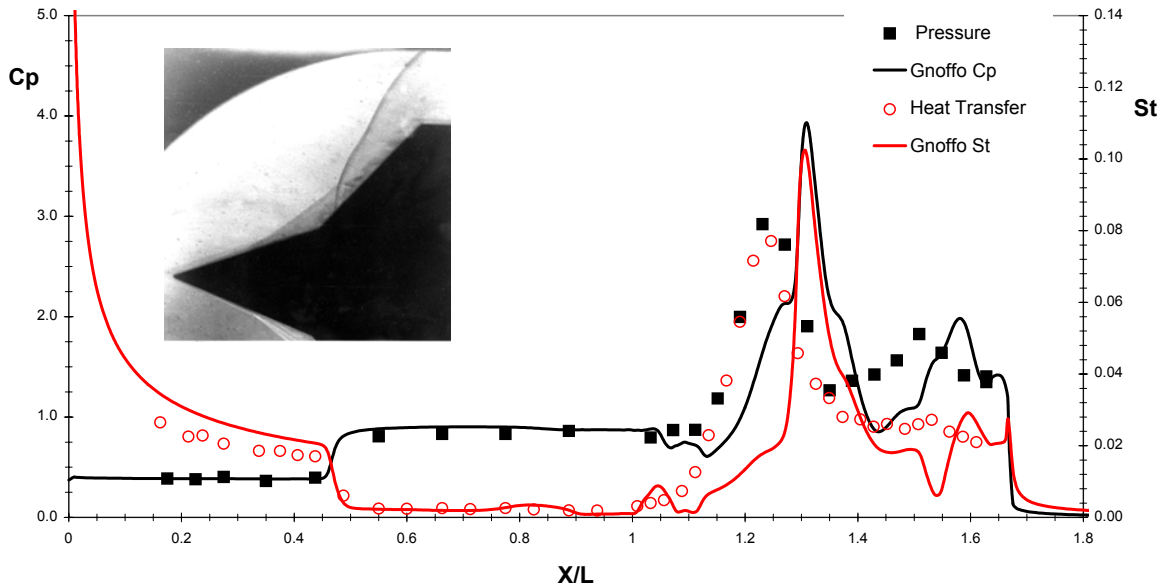


**Figure 48: Pressure, Heat Transfer and Schlieren Photo.  
Run 24 ( $M = 10.4$ ,  $Re_{\#}/ft = 10.4E+04$ ) : Gnoffo.**

*Measurements for Run 26*

Although we did not receive predictions for Run 26, the sharp double cone configuration run at Mach number of 10.4 and a Reynolds number of  $8.0 \times 10^4$ , the well-defined flowfield generated under these conditions could well be used for code validation. As in the earlier test cases, there are well-defined regions of constant pressure both upstream and downstream of the interaction region and the peak pressure and heat transfer in the shock/shock interaction region are well defined. The Schlieren photograph in Figure 49 shows well-defined features of the separation and afterbody shocks including a type IV interaction induced by the interaction between the separation shock and the afterbody shock.

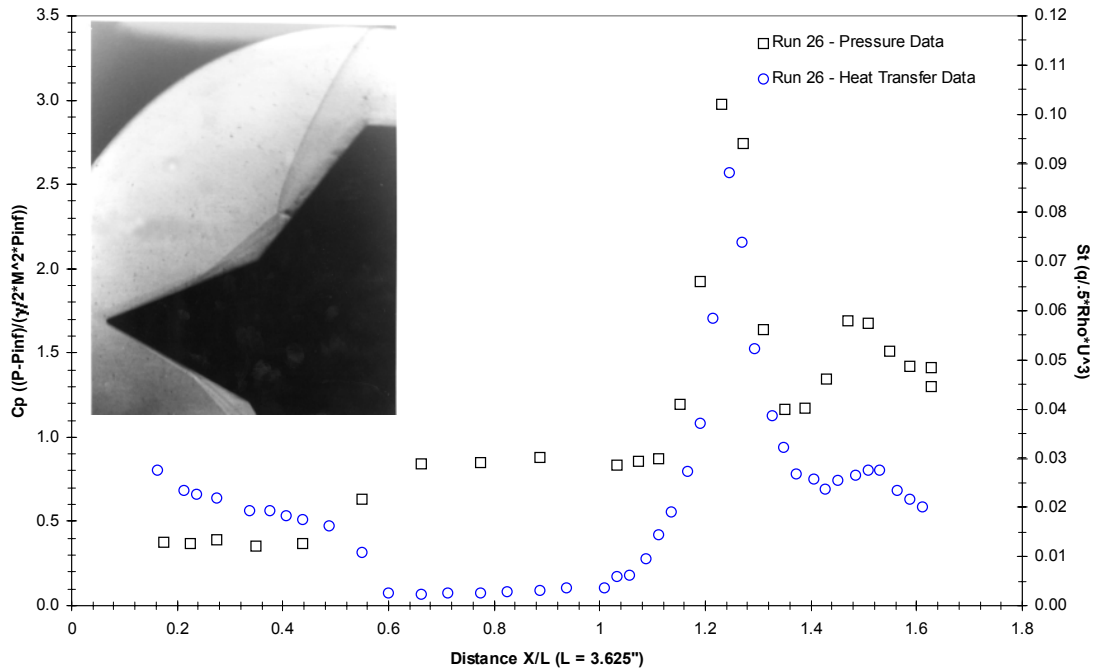


**Figure 49: Pressure, Heat Transfer and Schlieren Photograph.  
For Run 26 ( $M = 10.3$ ,  $Re_{\#}/ft = 8E+04$ ).**

*Measurements for Blunt Nose Configurations  
Runs 32, 36, 33 and 38*

For completeness we have included three additional measurements for which we did not receive predictions (Figures 50-53). These cases, which were run at a nominal Mach number of 10, illustrate that the separated region increases significantly with increased unit Reynolds number as would be anticipated for fully laminar interaction regions. An examination of the variation of the heating at the end of the second cone with Reynolds number shows no evidence of boundary layer transition. Increasing the Mach number from 10 to 12 holding the same Reynolds number as Run 32 has remarkably little influence on the size of the separated region, a result which was unexpected. For Run 38, well-defined characteristics of this flow would make it suitable for comparison with prediction.

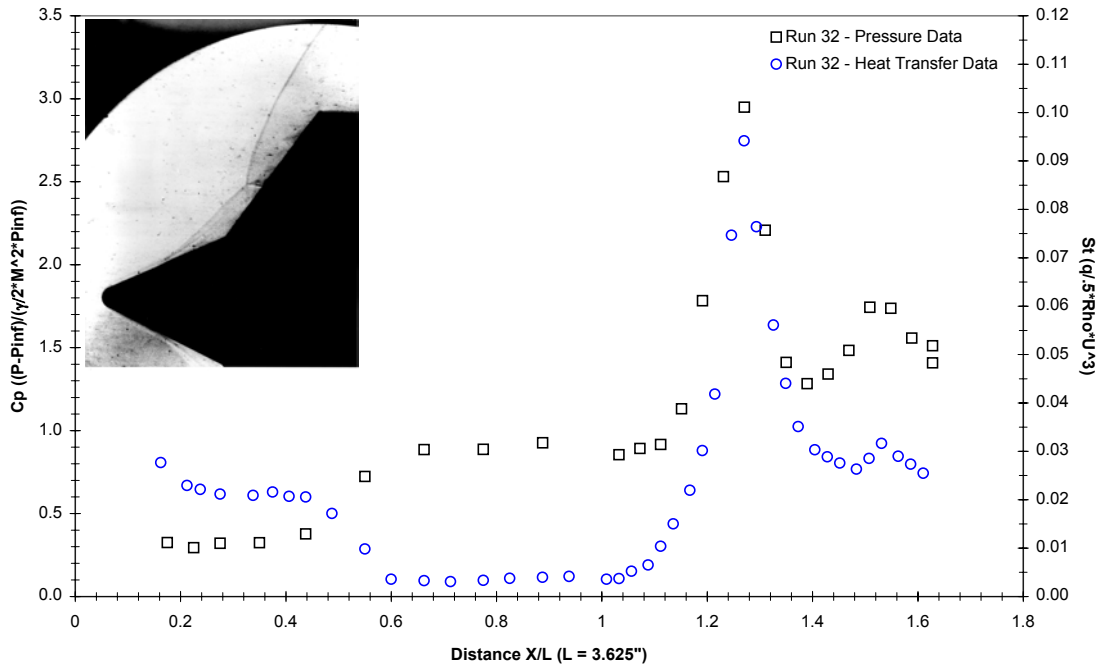


Figure 50: Pressure, Heat Transfer, and Schlieren Photograph.  
For Run 32 ( $M = 10.4$ ,  $Re\#/ft = 6E+04$ ).

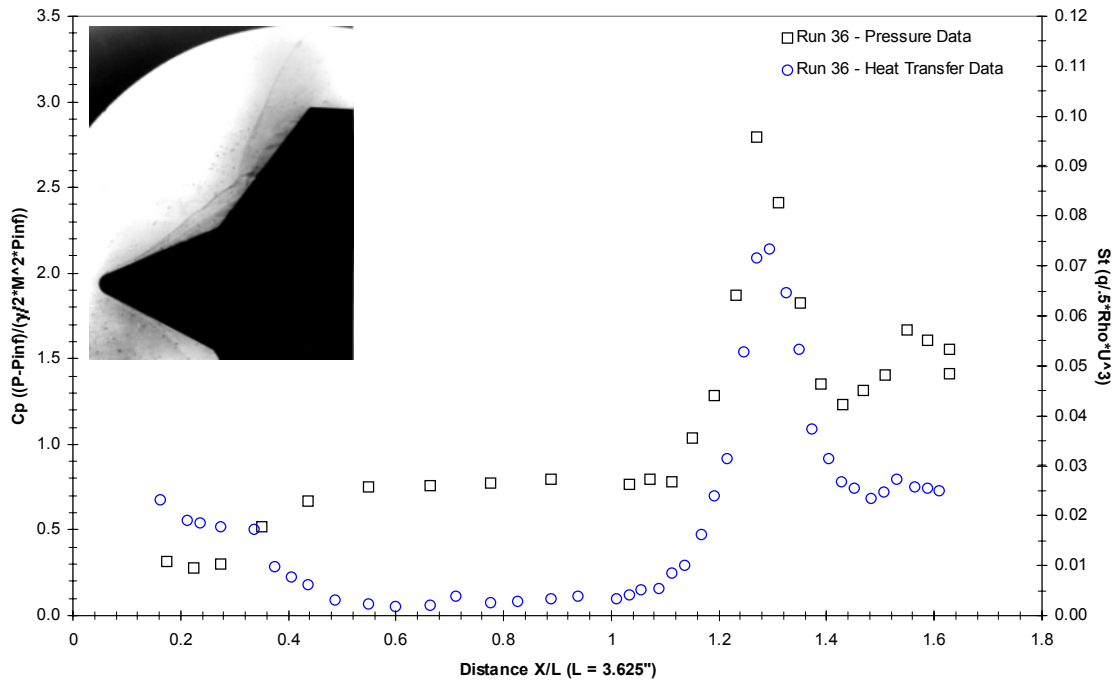


Figure 51: Pressure, Heat Transfer, and Schlieren Photograph.  
For Run 36 ( $M = 10.3$ ,  $Re\#/ft = 8E+04$ ).

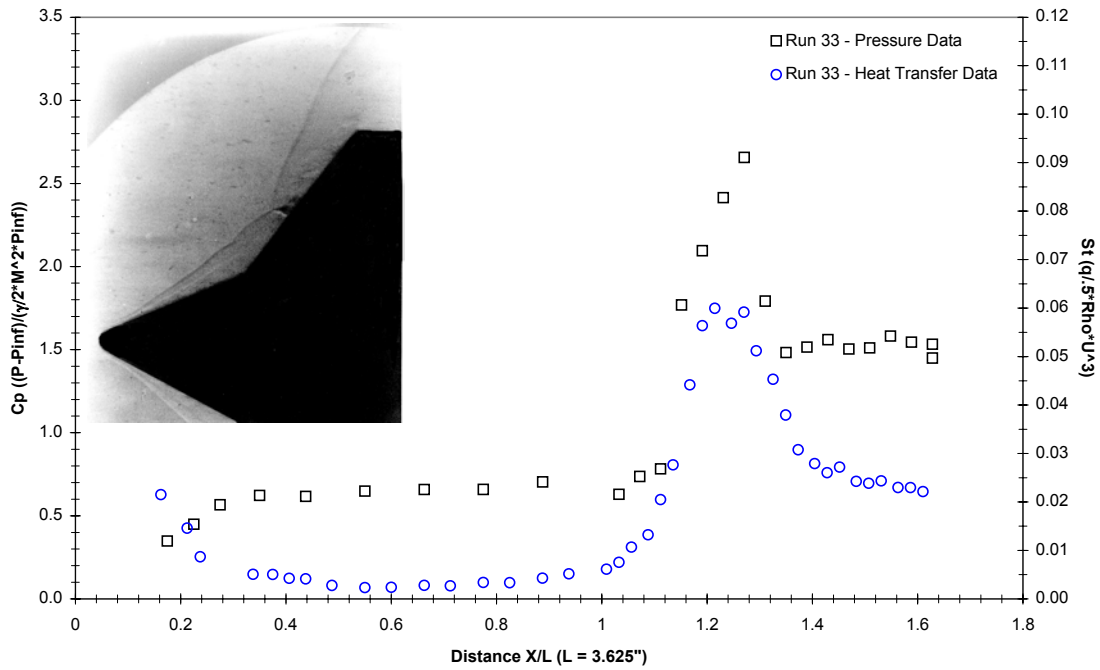


Figure 52: Pressure, Heat Transfer, and Schlieren Photograph. For Run 33 ( $M = 10.3$ ,  $Re_{\#}/ft = 9E+04$ ).

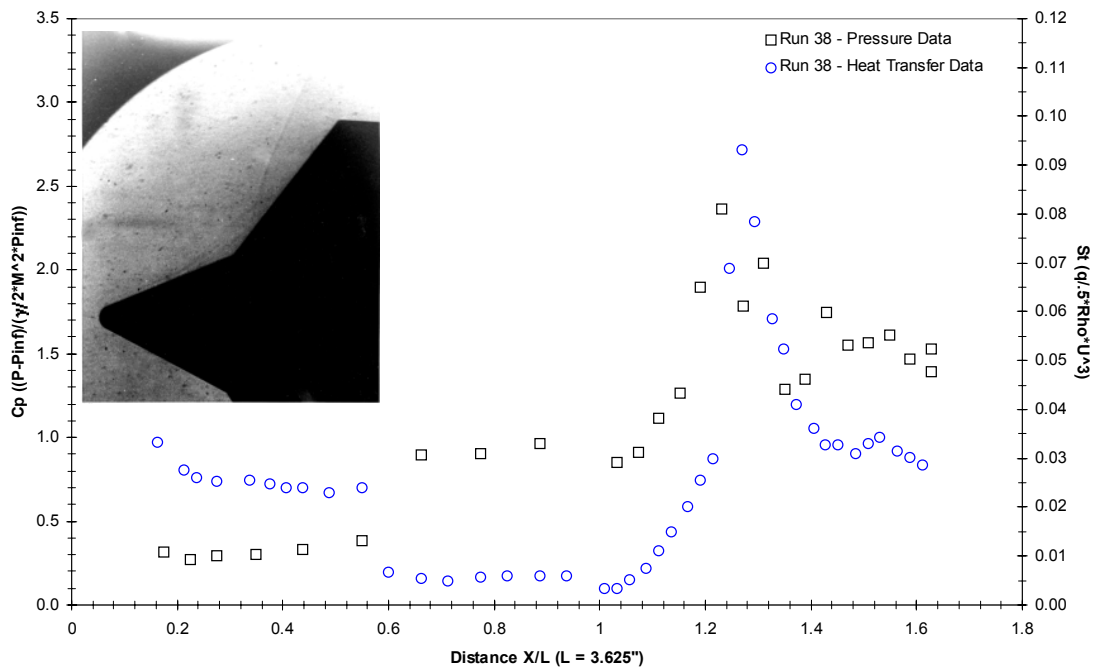


Figure 53: Pressure, Heat Transfer, and Schlieren Photograph. For Run 38 ( $M = 12.4$ ,  $Re_{\#}/ft = 6E+04$ ).

### 3.3 Measurements and Comparison with Hollow Cylinder/Flare Models

#### 3.3.1 Introduction

The experimental program with the hollow cylinder/flare configurations was conducted in two phases – the first sets of measurements were obtained with the extended flare configuration. Then when we had selected the freestream conditions, which gave interaction regions with the best-defined characteristics, we conducted the second phase of the program at these conditions, with the original French cone/flare configuration. The run matrix for the measurements on the hollow cylinder/flare configuration with the extended flare and the basic flare configuration are listed in Tables IIIA and IIIB respectively. These studies were preceded by detailed flowfield calibrations at each of the freestream conditions selected for the experiments. For the “blind” calibration study reported in Reference 6, fifteen computations for the hollow cylinder/flare model were submitted covering seven test cases. A majority of the solutions – eleven in all – were for the extended flare configuration. Almost all the predictions gave excellent results for the density contours over the model when compared with the Schlieren photographs. Figure 54 shows the density contours predicted by Gnoffo superimposed on the Schlieren photograph of the flow. The characteristics of the separated region as well as the shock waves developed over the leading edge and in the reattachment compression surface are well predicted by the Navier-Stokes solution.

**Table IIIA: Hollow Cylinder/Extended Flare Configuration**

Run	Po psia	Ho (ft/sec) <sup>2</sup>	Po' psia	Uinf ft/sec	Rhoinf slugs/ft <sup>3</sup>	Pinf psia	Tinf deg. R	Tvinf deg. R	M	Re/ft
2	667	4.07E+07	1.68	8.39E+03	3.73E-06	1.24E-02	2.70E+02	4.55E+03	10.24	1.45E+05
3	422	3.73E+07	1.11	7.98E+03	2.72E-06	8.33E-03	2.48E+02	4.57E+03	10.16	1.09E+05
8	1150	3.98E+07	1.14	8.36E+03	2.55E-06	5.69E-03	1.81E+02	4.48E+03	12.46	1.46E+05
9	749	3.69E+07	0.745	8.01E+03	1.81E-06	3.70E-03	1.66E+02	4.48E+03	12.49	1.09E+05
11	432	3.80E+07	0.46	8.10E+03	1.10E-06	2.38E-03	1.76E+02	4.75E+03	12.23	6.25E+04
12	709	3.81E+07	0.713	8.14E+03	1.68E-06	3.57E-03	1.73E+02	4.57E+03	12.44	9.86E+04
13	366	3.87E+07	0.896	8.13E+03	2.11E-06	6.51E-03	2.50E+02	4.50E+03	10.32	8.59E+04
14	251	3.36E+07	0.625	7.56E+03	1.71E-06	4.57E-03	2.17E+03	4.44E+0.3	10.30	7.38E+04

**Table IIIB: Hollow Cylinder/Short Flare Configuration**

Run	Po psia	Ho (ft/sec) <sup>2</sup>	Po' psia	Uinf ft/sec	Rhoinf slugs/ft <sup>3</sup>	Pinf psia	Tinf deg. R	Tvinf deg. R	M	Re/ft
18	1140	3.95E+07	1.11	8.33E+03	2.50E-06	5.56E-03	1.80E+02	4.45E+03	12.44	1.43E+05
19	772	3.71E+07	0.763	8.04E+03	1.84E-06	3.83E-03	1.68E+02	4.48E+03	12.42	1.10E+05
21	448	3.73E+07	1.11	7.99E+03	2.71E-06	8.17E-03	2.44E+02	4.57E+03	10.26	1.11E+05
22	604	3.90E+07	1.5	8.19E+03	3.49E-06	1.10E-02	2.56E+02	4.52E+03	10.27	1.39E+05
23	650	3.91E+07	0.675	8.23E+03	1.55E-06	3.41E-03	1.78E+02	4.68E+03	12.38	8.93E+04



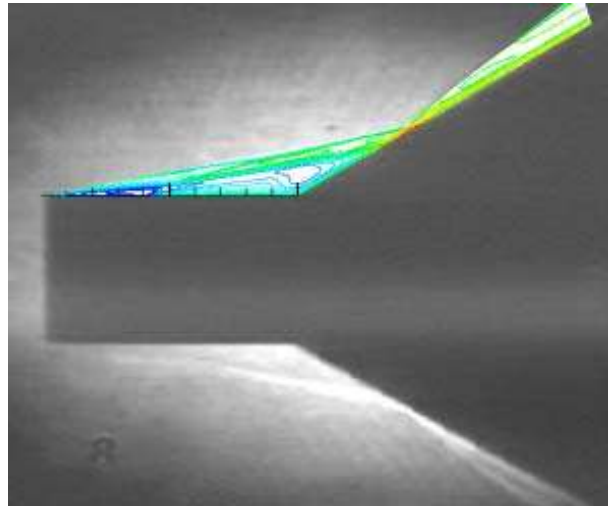


Figure 54: Run 8 Schlieren Photo with Density Contours of Gnoffo.  
( $M = 12.3$ ,  $Re\#/ft = 12E+04$ ).

### 3.3.2 Measurements for Hollow Cylinder/Extended Flare Models and Comparison with Predictions

#### *Comparison with Measurements for Run 14*

We received the most predictions for Run 14, which is an extended flare case conducted in a Mach number of 10.3 and an intermediate Reynolds number of  $7.8 \times 10^4$ . We have received two solutions from Candler, one with calculations for the original set of conditions and a second, where vibrational nonequilibrium was computed along the nozzle and in the test flow. Figure 55 shows these two predictions compared with the measurements of heat transfer and pressure obtained over the model. While the flows in the recirculation and reattachment compression region were computed with roughly equal accuracy with and in the absence of vibrational nonequilibrium, the pressure and heat transfer measurements over the hollow cylinder ahead of the interaction region are calculated well with and without including vibrational nonequilibrium effects.

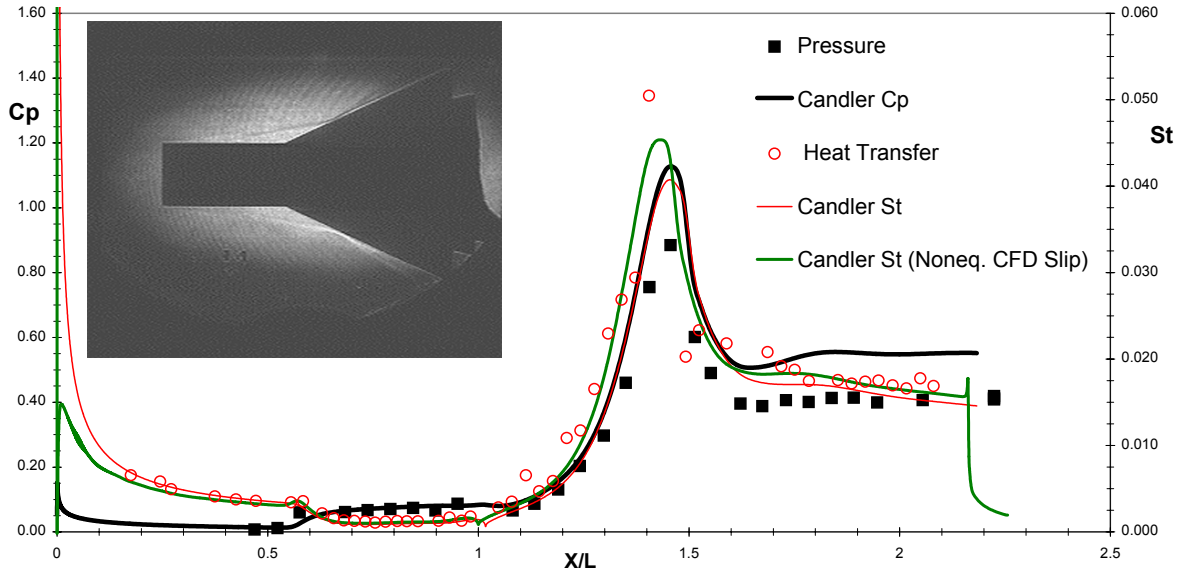


Figure 55: Pressure, Heat Transfer and Schlieren Photo Run 14.  
( $M = 10.3$ ,  $Re\#/ft = 7.83E+04$ ) : Candler.

Gnoffo's calculations (Figure 56) for this test case are in almost perfect agreement with the length of the interaction regions and the pressure and heat transfer measurements.

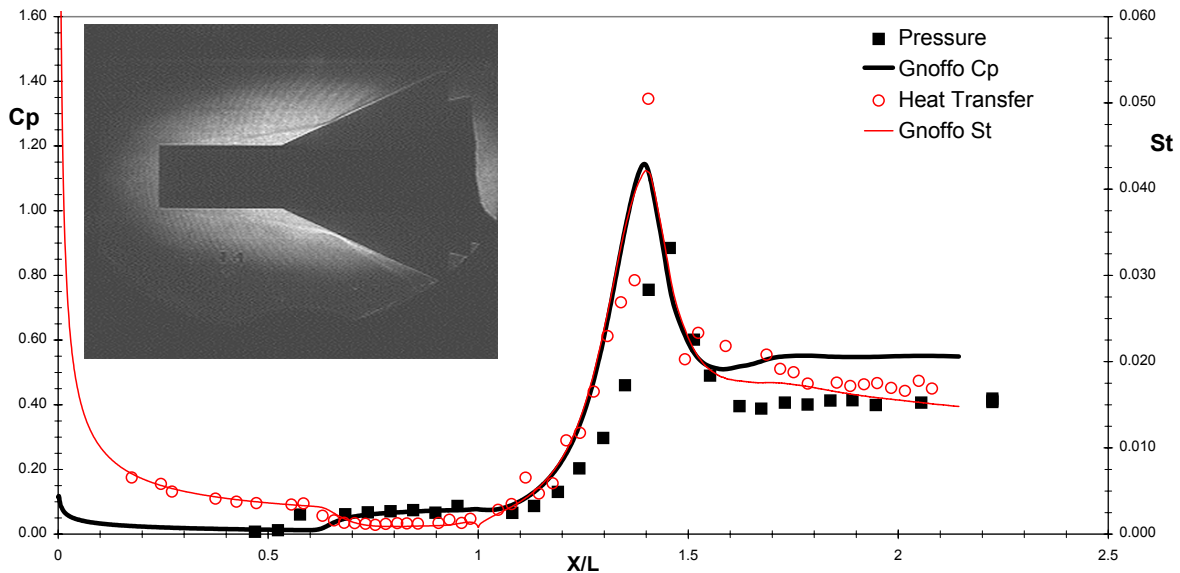


Figure 56: Pressure, Heat Transfer and Schlieren Photo Run 14.  
( $M = 10.3$ ,  $Re\#/ft = 7.83E+04$ ) : Gnoffo.

Surprisingly, the calculations of Tannehill (Figure 57) underpredict the length of separated region and the pressures and heat transfer in the forebody and reattachment region of the flow are reproduced well.

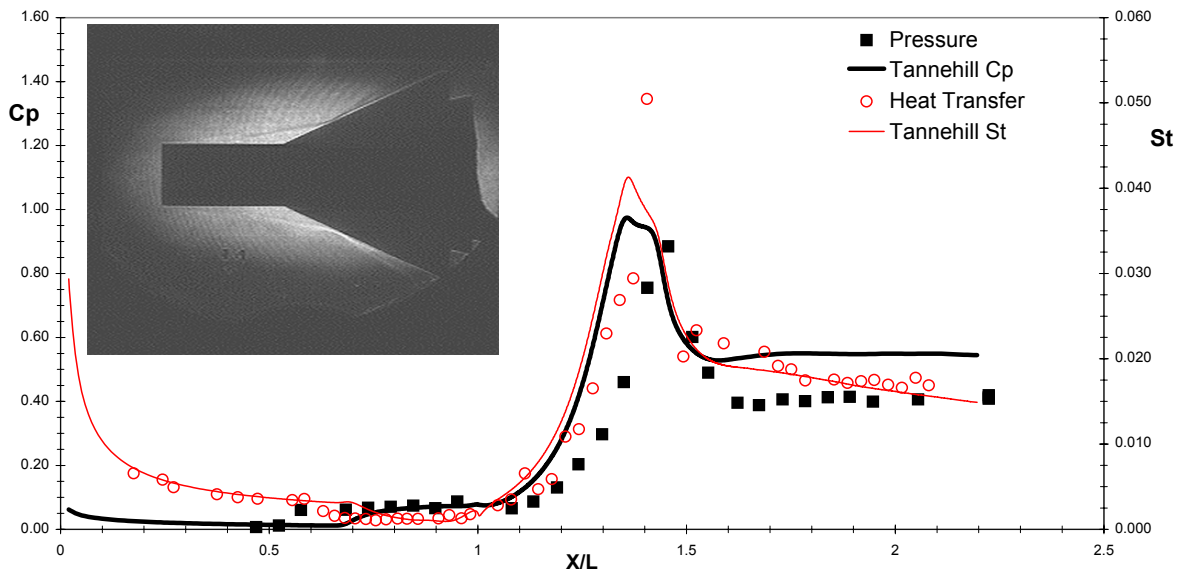


Figure 57: Pressure, Heat Transfer and Schlieren Photo Run 14.  
( $M = 10.3$ ,  $Re\#/ft = 7.83E+04$ ) : Tannehill.

*Comparison with Measurements for Run 9*

Run 9 was conducted under the highest Reynolds number, ( $10.9 \times 10^4$ ) Mach 12.5 condition, and for this case, the “blind” calculations of Gnoffo are almost in total agreement with the measurements. As shown in Figure 58, the length of separated region and the peak pressure and peak heating at the end of the reattachment and compression process are calculated almost exactly.

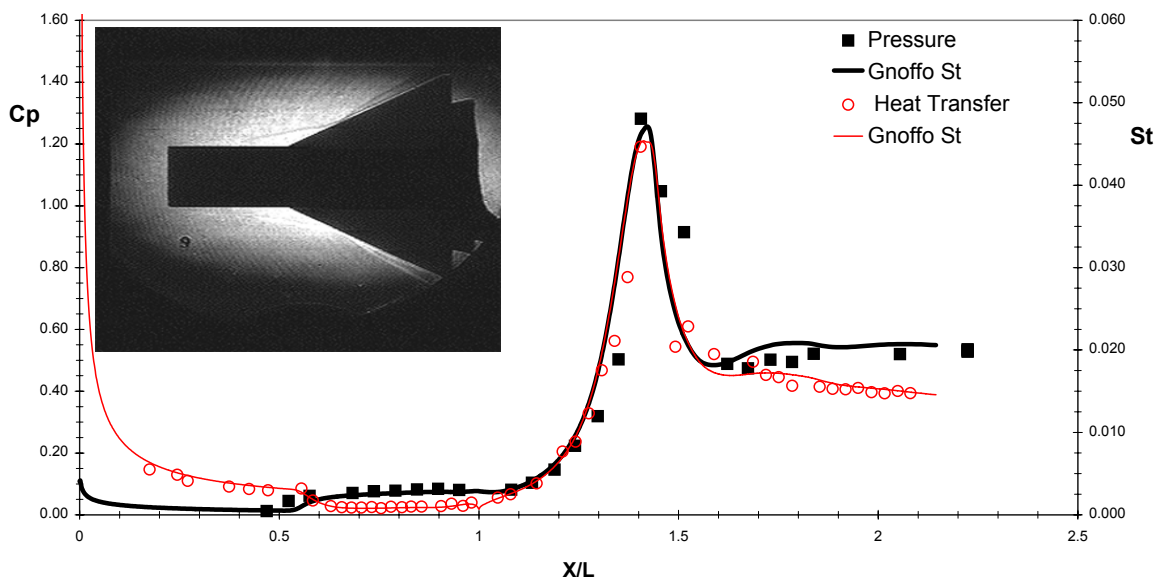


Figure 58: Pressure, Heat Transfer and Schlieren Photo.  
Run 9 ( $M = 12.48$ ,  $Re\#/ft = 10.9E+04$ ) : Gnoffo.

Not surprisingly, the predictions with the DSMC calculations obtained by Moss (Figure 59) follow the generally observed trend and underpredict the length of the separated region although the pressure and heating levels through and downstream of the interaction agree quite well with the measurements.

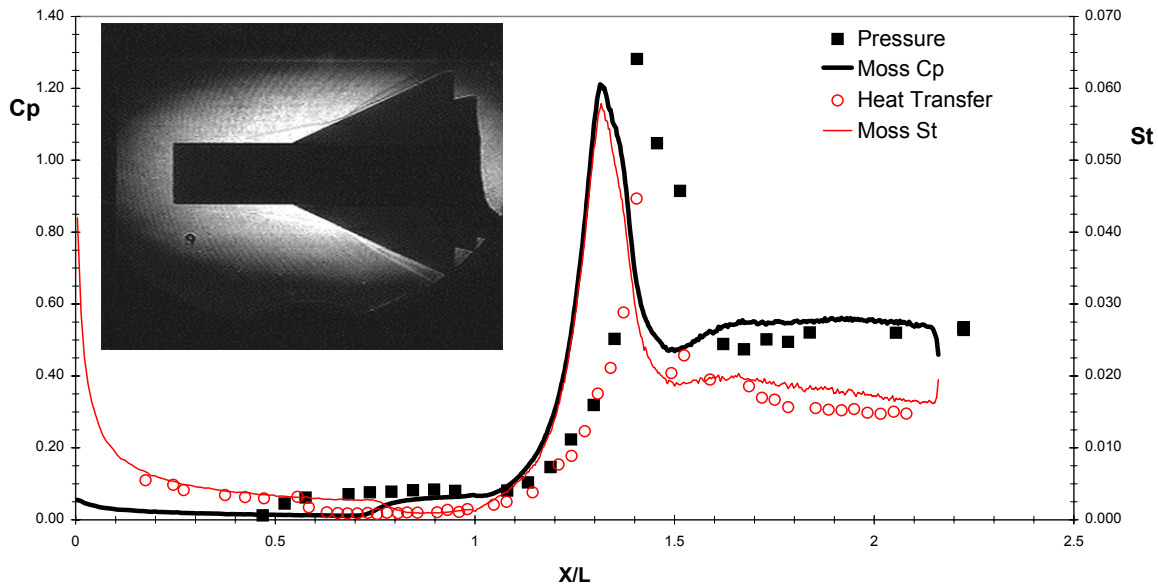


Figure 59: Pressure, Heat Transfer and Schlieren Photo.  
Run 9 ( $M = 12.48$ ,  $Re\#/ft = 10.9E+04$ ) : Moss.

#### Comparison with Measurements for Run 11

The flow conditions for Run 11 (Mach Number 12.2 and Reynolds number of  $6.3 \times 10^4$ ) were such that the flow was close to incipient separation and a very small recirculation region was present. As shown in Figure 60, while Candler's prediction of the forebody flow achieves reasonable agreement with experiment when vibrational nonequilibrium effects are included, the predicted length of separated region also increases. Likewise, as shown in Figure 62, Gnoffo's Navier-Stokes calculation also overpredicts the size of the recirculation region although the values for heat transfer and pressure are in relatively good agreement everywhere except the recirculation region. Tannehill's calculations (Figure 61) are in good agreement with the size of the separated region and the pressure level through the interaction region.

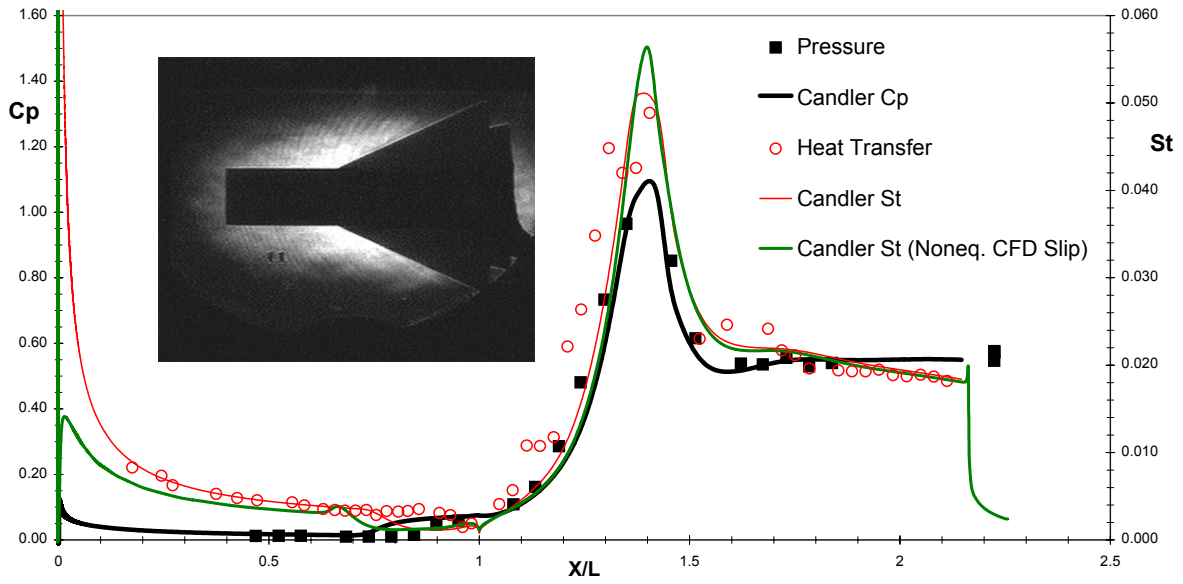


Figure 60: Pressure, Heat Transfer and Schlieren Photo.  
Run 11 ( $M = 12.23$ ,  $Re\#/ft = 6.25E+04$ ) : Candler.

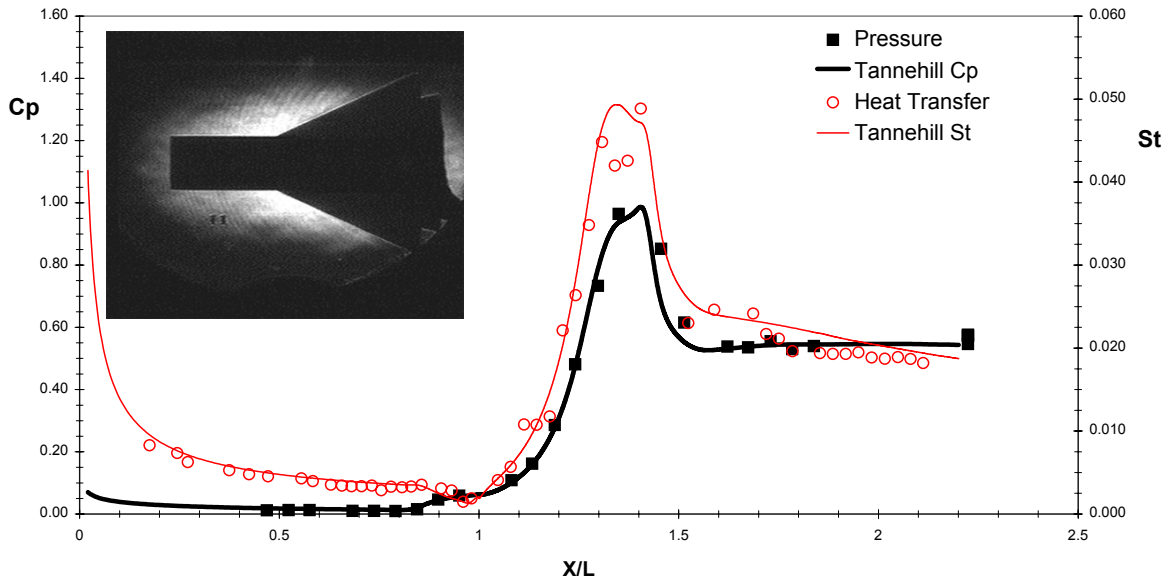


Figure 61: Pressure, Heat Transfer and Schlieren Photo.  
Run 11 ( $M = 12.23$ ,  $Re\#/ft = 6.25E+04$ ) : Tannehill.

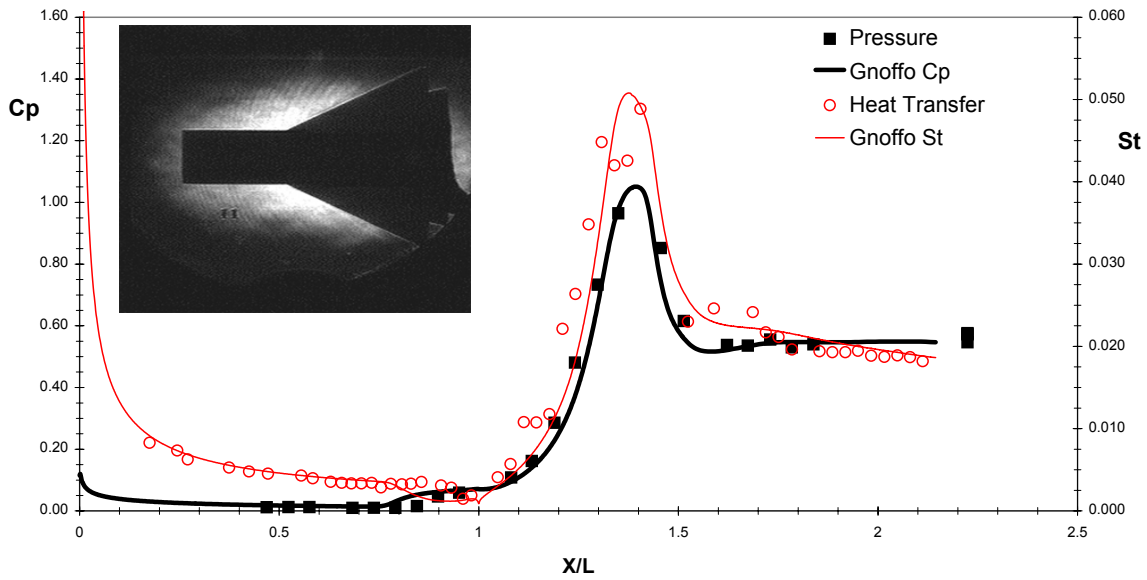


Figure 62: Pressure, Heat Transfer and Schlieren Photo.  
Run 11 ( $M = 12.23$ ,  $Re\#/ft = 6.25E+04$ ) : Gnoffo.

Moss's calculations using the DSMC method shown in Figure 63 also predict closely the small size of the interaction region and the heating and pressure distribution of the entire flow are well predicted. This appears to confirm that the basic problem with the DSMC computations rests in an inability to fix the length of the separation region; for the case very close to incipient separation where the separation length is not an issue, the method is quite successful in determining the remainder of the flowfield.

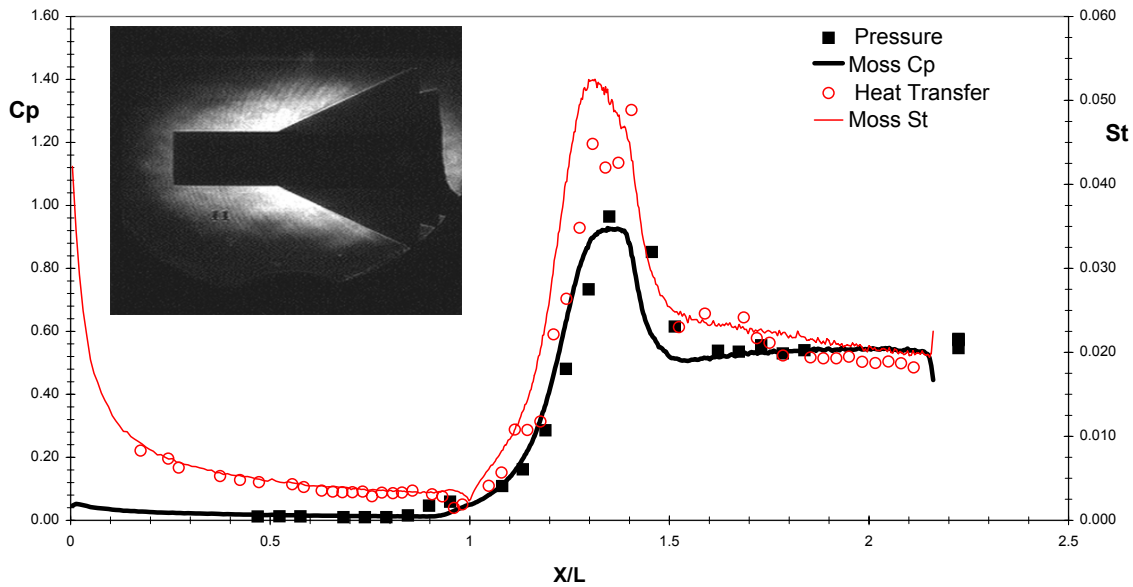


Figure 63: Pressure, Heat Transfer and Schlieren Photo.  
Run 11 ( $M = 12.23$ ,  $Re\#/ft = 6.25E+04$ ) : Moss.



Boyd's DSMC computations shown in Figure 64 are in agreement with the measured scale of the separated region and although the pressure predictions are in good agreement with the experiment, the method tends to underpredict the heating both ahead and downstream of the interaction region.

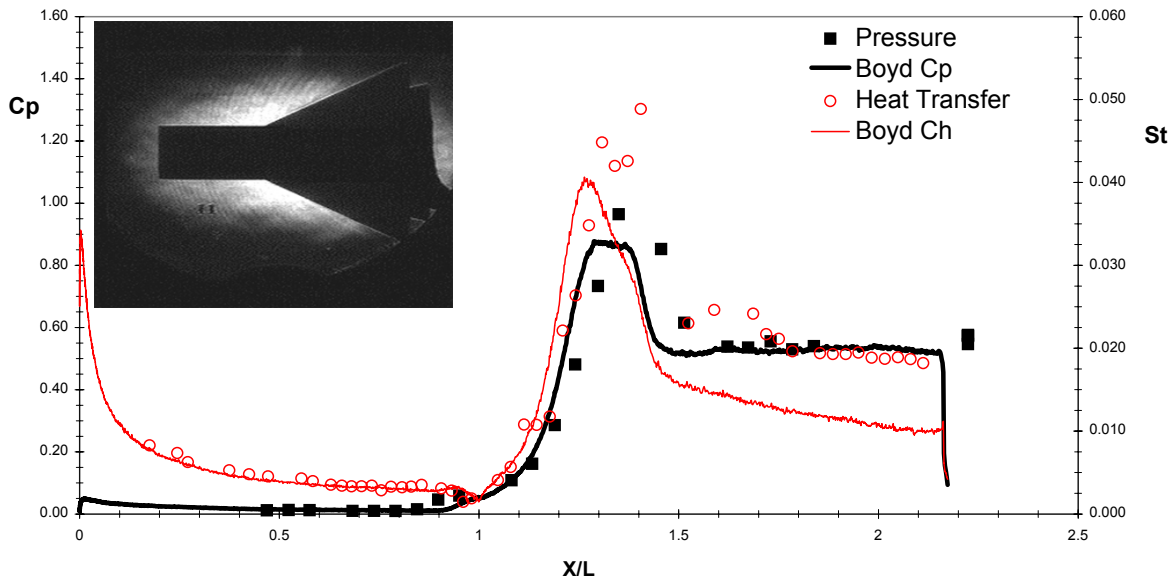


Figure 64: Pressure, Heat Transfer and Schlieren Photo.  
Run 11 ( $M = 12.23$ ,  $Re_{\#}/ft = 6.25E+04$ ) : Boyd.

#### Comparison with Measurements for Run 8

The high Reynolds number test conditions for Run 8 (Mach 12.5 and Reynolds number  $14.6 \times 10^4$ ) produced the largest separated region over the cylinder flare model and again Gnoffo's calculations shown in Figure 65 are almost in exact agreement with the experimental data, even capturing the peak pressure and peak heating levels at the end of the reattachment compression process.

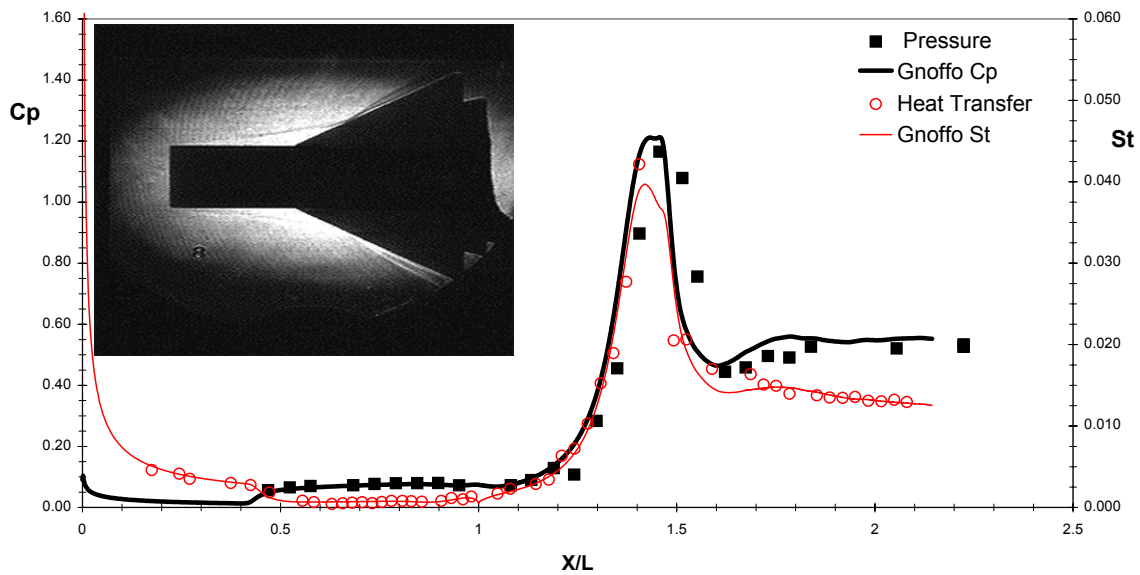


Figure 65: Pressure, Heat Transfer and Schlieren Photo.  
Run 8 ( $M = 12.46$ ,  $Re\#/ft = 14.6E+04$ ) : Gnoffo.

### 3.3.3 Measurements for Hollow Cylinder/Original Flare Models and Comparison with Predictions

#### Introduction

The dimensions of the hollow cylinder/short flare model were exactly those of the model tested earlier by Chanetz et al (Ref. 1). Computations of the flow over this configuration made earlier at the Antibes Workshop held in France in 1989 demonstrated that the solutions were extremely sensitive to the modeling of the flow over the leading edge, the gridding of the recirculation region and the differencing schemes used in this region of the flow. While in this flow configuration measurements made in the current studies suggest that reattachment occurs at the tip of the flare, the separated region is smaller than if the expansion fan were well downstream, as is in the case of the expanded flare. Again, as shown in Figure 66, the computation of density contours over the model computed by Gnoffo for Run 18 are in excellent agreement with experiment.

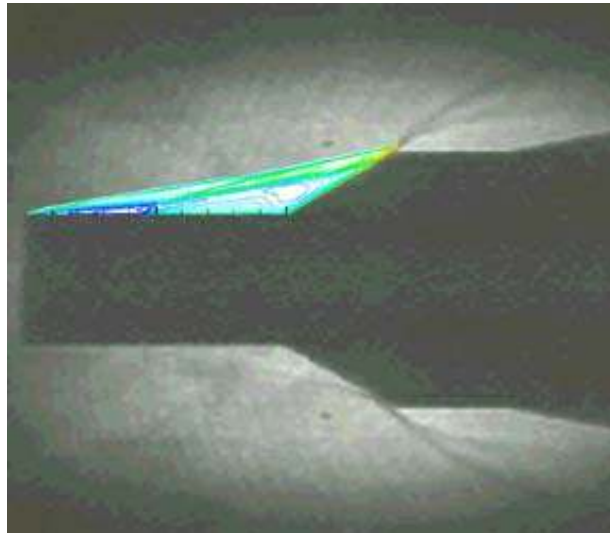


Figure 66: Hollow Cylinder with Short Flare – Run 18. Composite picture showing Schlieren image and Density contour computed by Gnoffo.

*Comparison with Measurements for Run 18*

For this test case, which was conducted at the largest Reynolds number ( $14.3 \times 10^4$ ) at Mach 12.5, we obtain the large separated region. Gnoffo's predictions for this condition shown in Figure 67 again are in good agreement with the experimental data, almost capturing the length of the interaction region and the magnitude of heat transfer and pressure throughout the flow. Clearly the lessons from the Antibes and subsequent code validation studies have been learned.

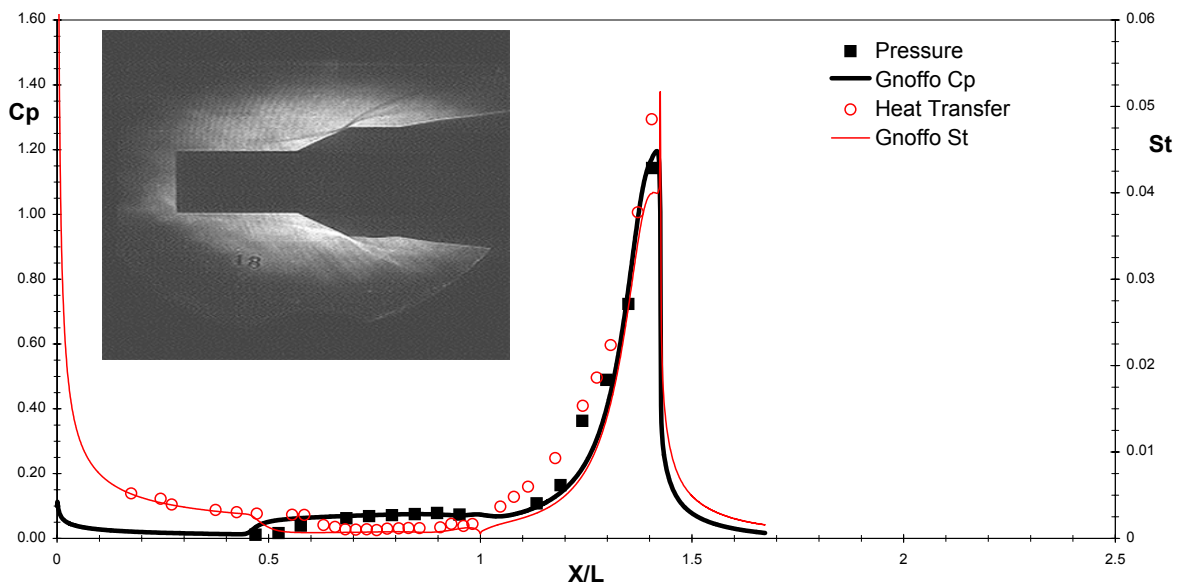
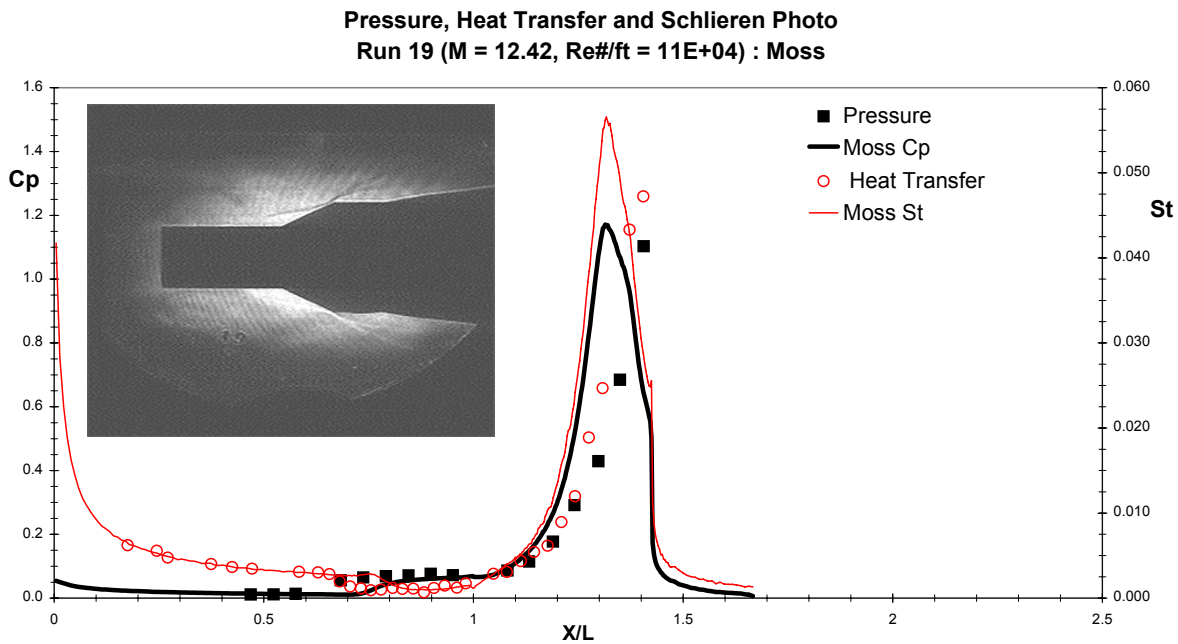


Figure 67: Pressure and Heat Transfer. Run 18 ( $M = 12.44$ ,  $Re_{\#}/ft = 14.3E+04$ ) : Gnoffo.

*Comparison with Measurements for Run 19*

With DSMC computation for the short-flare case, at an intermediate Reynolds number of  $7.92 \times 10^4$ , the calculations made by Moss are in relatively good agreement with the measurements of heat transfer and pressure. Moss predicts a shorter interaction region and this results in a peak in the pressure and heat transfer before the end of the flare as shown in Figure 68.



**Figure 68: Pressure and Heat Transfer.**  
**Run 19 (M = 12.42, Re#/ft = 11.0E+04) : Moss.**

## 4 CONCLUSIONS

In this section of the RTO/AVT activity we examined the capabilities of the Navier-Stokes and DSMC prediction techniques to describe accurately the aerothermal characteristics of complex laminar viscous flows generated in regions of shock wave/boundary layer interaction and shock/shock interaction in hypervelocity flows. Two simple axisymmetric body shapes were selected for these studies, a hollow cylinder/flare configuration, and double cone configuration, each of which has been shown to generate flow which can stress the computation techniques. Experimental studies in which detailed heat transfer and pressure measurements were made in hypervelocity flows at Mach numbers of 10 and 12 over a range of Reynolds numbers low enough to ensure the flows remained laminar over the models, and that both Navier-Stokes and DSMC methods could be employed to calculate the flows. The measurements from these experimental studies were first released in a “blind validation study” where the predictors were given only the model geometry and the conditions in the freestream so, other than conferring with each other, they had no knowledge of the results. Based on their earlier experience the participants expressed misgivings about the accuracy of the predictions, particularly for the double cone cases where both the gridding and the selection of the differencing schemes proved to be of critical importance. However, this blind validation exercise demonstrated the best computationalist can make sound decisions and the accuracy of most of the predictions

were truly impressive. In the best Navier-Stokes solutions the structure and density of the flowfield was captured exactly over both the hollow cylinder/flare and double cone models. The detailed characteristics of the distribution of pressure and heating through the interaction regions were well predicted. In general, for these relatively high-density flows, the DSMC solutions did not capture the characteristics of well-separated flows. The slight disagreement with the heating on the forebody of the double cone models stimulated in a second experimental investigation to examine the effects of vibrational non-equilibrium on freestream conditions and on the forebody heating. This study was performed in concert with numerical analysis of the flow in the nozzle and over the cylinder and cone models using both simple and detailed Navier-Stokes modeling. The combined set of flowfield and model measurements were then used to validate the calculations of the freestream conditions in the presents of vibrational nonequilibrium. Comparisons between the computations and the experimental data evaluated with the updated freestream conditions improved the already good agreement between prediction and experiment.

## 5 REFERENCES

- [1] Chanetz, B., R. Benay, J-M. Bousquet, R. Bur, T. Pot, F. Grasso, and J.N. Moss, "Experimental and Numerical Study of the Laminar Separation in Hypersonic Flow," *Aerospace Science and Technology*, No. 3, 1998, pp. 205-218.
- [2] Olejniczak, J., Candler, G.V., "Computation of Hypersonic Shock Interaction Flow Fields," 7th AIAA/ASME Joint Thermophysics and Heat Transfer Conference, AIAA Paper 98-2446, June 1998.
- [3] Gnoffo, Peter, private communication, 1999.
- [4] Holden, Michael, "Shock Interaction in Hypersonic Flows," AIAA Paper 98-2751, presented at 29th Plasmadynamics and Laser Conference, Albuquerque, NM, June 15-18, 1998.
- [5] Holden, Michael S. and Wadhams, Timothy P., "Code Validation Study of Laminar Shock/Boundary Layer and Shock/Shock Interactions in Hypersonic Flow, Part A: Experimental Measurements", AIAA 2001-1031, 39<sup>th</sup> Aerospace Sciences Meeting & Exhibit, January 8-12, 2001, Reno, NV.
- [6] Harvey, John K., Holden, Michael S., and Wadhams, Timothy P., "Code Validation Study of Laminar Shock/Boundary Layer and Shock/Shock Interactions in Hypersonic Flow, Part B: Comparison with Navier-Stokes and DSMC Solutions," AIAA 2001-1031, 39<sup>th</sup> Aerospace Sciences Meeting & Exhibit, Reno, NV, January 8-12, 2001.
- [7] Candler, Graham V., Nompelis, Ioannis, Druguet, Marie-Claude, Boyd, Iain D., Wang, Wen-Lan, Holden, Michael S., "CFD Validation for Hypersonic Flight: Hypersonic Double-Cone Flow Simulations," AIAA 2002-0581, presented at 40<sup>th</sup> Aerospace Sciences Meeting & Exhibit, January 13-17, 2002, Reno, NV.
- [8] Gnoffo, Peter, Private Communication, 2001.
- [9] Hall, J.G., and Treanor, C.E., "Non-equilibrium Effects in Supersonic Nozzle Flows," CAL Report No. CAL-163, March 1968.
- [10] Boudreau, Albert H., "Characterization of Flow Fields in Hypersonic Ground Test Facilities," **Methodology of Hypersonic Testing**, Lecture Series 1993-03, von Karman Institute for Fluid Dynamics, pp. 4-1 – 4-15.

- [11] Millikan, R.C. and White, D.R., "Systematics of Vibrational Relaxation," *Journal of Chemical Physics*, Vol. 39, 1963, pp. 3209-3213.
- [12] Lordi, John, private communication, 2001-2002.
- [13] Lordi, J.A., Mates, R.E. and Moselle, J.R., "Computer Program for the Numerical Solution of Nonequilibrium Expansions of Reacting Gas Mixtures," Cornell Aeronautical Report No. AD-1689-A-6, NASr-109, October 1965.
- [14] Candler, G.V., Nompelis, I., Druguet, M-C., "Navier-Stokes Predictions of Hypersonic Double-Cone and Cylinder-Flare Flow Fields," AIAA Paper No. 2001-1024, January 2001, AIAA 39<sup>th</sup> Aerospace Sciences Meeting & Exhibit, Reno, NV, January 8-12, 2001.
- [15] Boyd, I.D., and Wang, W-L., "Monte Carlo Computations of Hypersonic Interacting Flows," AIAA Paper No. 2001-1029, 39<sup>th</sup> Aerospace Sciences Meeting and Exhibit, Reno, NV, January 8-12, 2001.
- [16] Cheng, H.K., Hall, J. Gordon, Golian, T.C., and Hertzberg, A., "Boundary Layer Displacement and Leading Edge Bluntness Effects in High-Temperature Hypersonic Flow," *Journal of the Aerospace Sciences*, Vol. 28, No. 5, May 1961. Also presented at Hypersonic Phenomena Session, IAS 28<sup>th</sup> Annual Meeting, NY, January 25-27, 1960.
- [17] Gaitonde, Datta V., "Evaluation of Flux-Split Schemes in Laminar Hypersonic Flows," oral presentation, Reno, NV, January 2001.
- [18] Gnoffo, Peter, "CFD Validation Studies for Hypersonic Flow Prediction," AIAA 2001-1025, 39<sup>th</sup> Aerospace Sciences Meeting and Exhibit, Reno, NV, January 8-12, 2001.
- [19] Moss, James, "DSMC Computations for Regions of Shock/Shock and Shock/Boundary Layer Interaction," AIAA 2001-1027, 39<sup>th</sup> Aerospace Sciences meeting and Exhibit, Reno, NV, January 8-12, 2001.
- [20] Roy, Christopher J., Gallis, Michael A., Payne, Jeffrey L., and Bartel, Timothy J., "Navier-Stokes and DSMC Simulations for Hypersonic Laminar Shock/Shock Interaction Flows," presented at the AIAA 40<sup>th</sup> Aerospace Sciences Meeting and Exhibit, Reno, NV, January 14-17, 2002.
- [21] Gallis, M., Roy, C., Payne, J. and Bartel, T., "DSMC and Navier-Stokes Predictions for Hypersonic Laminar Interacting Flows," AIAA 2001-1030, 39<sup>th</sup> Aerospace Sciences Meeting and Exhibit, Reno, NV, January 8-12, 2001.
- [22] Kato, H. and Tannehill, J., "Computation of Hypersonic Laminar Separated Flows using an Iterated PNS Algorithm," AIAA 2001-1028, 39<sup>th</sup> Aerospace Sciences Meeting and Exhibit, Reno, NV, January 8-12, 2001.